



## **NRLMSIS 2.1: An Empirical Model of Nitric Oxide Incorporated Into MSIS**

Downloaded from: <https://research.chalmers.se>, 2025-12-04 23:34 UTC

Citation for the original published paper (version of record):

Emmert, J., Jones, M., Siskind, D. et al (2022). NRLMSIS 2.1: An Empirical Model of Nitric Oxide Incorporated Into MSIS. *Journal of Geophysical Research: Space Physics*, 127(10).  
<http://dx.doi.org/10.1029/2022JA030896>

N.B. When citing this work, cite the original published paper.

# JGR Space Physics

## RESEARCH ARTICLE

10.1029/2022JA030896

### Key Points:

- New nitric oxide (NO) component of NRLMSIS empirical temperature and density model, from ~73 km to exobase
- Constructed within NRLMSIS 2.0 framework; NO density is coupled to MSIS temperature above ~110 km
- The empirical fit is based on observations from six space-based instruments

### Supporting Information:

Supporting Information may be found in the online version of this article.

### Correspondence to:

J. T. Emmert,  
[john.emmert@nrl.navy.mil](mailto:john.emmert@nrl.navy.mil)

### Citation:

Emmert, J. T., Jones, M. Jr., Siskind, D. E., Drob, D. P., Picone, J. M., Stevens, M. H., et al. (2022). NRLMSIS 2.1: An empirical model of nitric oxide incorporated into MSIS. *Journal of Geophysical Research: Space Physics*, 127, e2022JA030896. <https://doi.org/10.1029/2022JA030896>







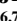





Received 2 AUG 2022

Accepted 9 SEP 2022

© 2022 The Authors. This article has been contributed to by U.S. Government employees and their work is in the public domain in the USA.

This is an open access article under the terms of the [Creative Commons Attribution-NonCommercial License](https://creativecommons.org/licenses/by-nc/4.0/), which permits use, distribution and reproduction in any medium, provided the original work is properly cited and is not used for commercial purposes.

## NRLMSIS 2.1: An Empirical Model of Nitric Oxide Incorporated Into MSIS

J. T. Emmert<sup>1</sup> , M. Jones Jr.<sup>1</sup> , D. E. Siskind<sup>1,2</sup> , D. P. Drob<sup>1</sup> , J. M. Picone<sup>3</sup> , M. H. Stevens<sup>1</sup> , S. M. Bailey<sup>4,5</sup> , S. Bender<sup>6,7</sup> , P. F. Bernath<sup>8,9</sup> , B. Funke<sup>10</sup> , M. E. Hervig<sup>11</sup> , and K. Pérot<sup>12</sup> 

<sup>1</sup>Space Science Division, U.S. Naval Research Laboratory, Washington, DC, USA, <sup>2</sup>Now at Computational Physics, Inc., Springfield, VA, USA, <sup>3</sup>Voluntary Emeritus Program, U.S. Naval Research Laboratory, Washington, DC, USA, <sup>4</sup>Department of Electrical and Computer Engineering, Virginia Tech, Blacksburg, VA, USA, <sup>5</sup>Center for Space Science and Engineering Research, Virginia Tech, Blacksburg, VA, USA, <sup>6</sup>Department of Physics, Norwegian University of Science and Technology, Trondheim, Norway, <sup>7</sup>Birkeland Centre for Space Science, Bergen, Norway, <sup>8</sup>Department of Chemistry and Biochemistry, Old Dominion University, Norfolk, VA, USA, <sup>9</sup>Department of Chemistry, University of Waterloo, Waterloo, ON, Canada, <sup>10</sup>Instituto de Astrofísica de Andalucía, CSIC, Granada, Spain, <sup>11</sup>GATS, Driggs, ID, USA, <sup>12</sup>Department of Space, Earth and Environment, Chalmers University of Technology, Gothenburg, Sweden

**Abstract** We have developed an empirical model of nitric oxide (NO) number density at altitudes from ~73 km to the exobase, as a function of altitude, latitude, day of year, solar zenith angle, solar activity, and geomagnetic activity. The model is part of the NRLMSIS@ 2.1 empirical model of atmospheric temperature and species densities; this upgrade to NRLMSIS 2.0 consists solely of the addition of NO. MSIS 2.1 assimilates observations from six space-based instruments: UARS/HALOE, SNOE, Envisat/MIPAS, ACE/FTS, Odin/SMR, and AIM/SOFIE. We additionally evaluated the new model against independent extant NO data sets. In this paper, we describe the formulation and fitting of the model, examine biases between the data sets and model and among the data sets, compare with another empirical NO model (NOEM), and discuss scientific aspects of our analysis.

## 1. Introduction

Nitric oxide (NO) is one of the most important trace species in the Earth's thermosphere and plays a key role governing the structure of the atmosphere above 100 km. As a heteronuclear molecule, it figures prominently in the thermospheric energy budget through radiative emission in the 5.3  $\mu\text{m}$  band (Kockarts, 1980; Mlynarczyk et al., 2003, 2021; Zhang & Paxton, 2021). It is also a valuable diagnostic for energy input into the thermosphere, either from energetic particles at high latitude (Gérard & Barth, 1977; Hendrickx et al., 2015, 2017, 2018; Siskind et al., 1989) or from solar soft X-rays at low latitudes (Barth et al., 1988; Siskind et al., 1990, 1995). NO also responds to dynamical forcing and has been used to infer the variability of both nonmigrating (e.g., Oberheide & Forbes, 2008) and migrating (Siskind et al., 2019) tides. At lower altitudes, below 100 km, it is the dominant source of ionization of the quiet time D region ionosphere (Brasseur & Solomon, 2005; Nicolet & Aikin, 1960). Mesospheric NO, particularly at high winter latitudes where photodissociation minimizes, is of special interest because it can provide a means for coupling between the upper and middle atmosphere (Randall et al., 2007, 2015; Sinnhuber et al., 2016; Siskind et al., 2000; Solomon et al., 1982), potentially contributing to catalytic destruction of stratospheric ozone (Natarajan et al., 2004).

Despite this broad interest in NO, the existing climatologies and empirical models have been typically limited to specific data sets, each with its own spatiotemporal coverage limitations. (Note that the acronyms used below and throughout the paper are defined at the end of the text.) Early work by Siskind et al. (1998) used Solar Mesosphere Explorer and UARS/HALOE data to produce climatologies covering 50–160 km altitude (the measurements overlap from 98 to 125 km). Marsh et al. (2004) developed a 100–150 km empirical model, NO model (NOEM), based on 1998–2000 SNOE data. Kiviranta et al. (2018) created an empirical model, SANOMA, from Odin/SMR data and compared it with NOEM and with data from AIM/SOFIE, Envisat/SCIAMACHY, Envisat/MIPAS, and ACE/FTS. SANOMA covers altitudes 85–115 km and is constructed similarly to NOEM. Bender et al. (2019) presented an empirical model of 60–90 km SCIAMACHY data. Bender et al. (2015) compared averages of coincident daily means from SCIAMACHY, MIPAS, ACE, and SMR, collectively covering the height range 60–150 km.

In this paper, we describe a new empirical model of NO that is based on six data sets (SNOE, MIPAS, ACE, SOFIE, HALOE, and SMR) and is incorporated into the NRLMSIS® empirical model of atmospheric temperature and species densities. The model covers altitudes from ~73 km to the exobase (~500 km), which greatly expands the range of altitudes compared to previous empirical models and climatologies. It also assimilates more data (covering altitudes from 70 to 200 km), and more data sets, than previous models. The new model, designated NRLMSIS 2.1, is an upgrade to NRLMSIS 2.0 (Emmert et al. (2020), designated “M2.0” herein), the only change being the addition of NO. Herein, “NRLMSIS” is often shortened to “MSIS,” if the version is omitted, “MSIS” collectively refers to all versions of the model.

The NO formulation of MSIS 2.1 is described in Section 2. Section 3 describes the data sets used to tune and validate the model and details the random sampling procedure, and Section 4 describes the fitting procedure to estimate the model parameters. In Section 5, we examine in depth the climatological dependence of the model and underlying data on the independent geophysical variables (altitude, latitude, day of year, solar activity, geomagnetic activity, and local time). We also validate the model against the data, examine mutual biases among the data sets, and discuss accompanying scientific issues. Section 6 compares MSIS 2.1 with NOEM, and Section 7 compares the model with several historical rocket experiments. Section 8 summarizes the study, including the design of the new NO model embedded in MSIS 2.1, the climatological behavior of NO inferred via the MSIS assimilation, and the primary results of the comparison of MSIS 2.1 with NO measurements. Fortran code to run MSIS 2.1 is included in Supporting Information S3.

## 2. Model Formulation

The MSIS 2.1 formulation is the same as MSIS 2.0 but with the addition of an NO vertical profile parameterization and some additional solar activity expansion terms (which are currently only used for NO). In this section, we describe the mathematical treatment of the NO formulation.

### 2.1. Vertical NO Profile

The vertical NO profile is parameterized similarly to the atomic oxygen profile in MSIS 2.0. In terms of geopotential height  $\zeta$ , the profile is defined by the following:

$$\ln n(\zeta) = \begin{cases} \ln n_0 - \frac{g_0}{k} \int_{\zeta_0}^{\zeta} \frac{M(\zeta')}{T(\zeta')} d\zeta' - \ln \frac{T(\zeta)}{T(\zeta_0)} - C e^{-(\zeta - \zeta_C)/H_C} & ; \zeta \geq \zeta_0 \\ \sum_{i=0}^{N_S-1} \alpha_i S_i(\zeta) & ; \zeta < \zeta_0 \end{cases} \quad (1)$$

$T(\zeta)$	Temperature
$n(\zeta)$	Number density of NO
$n_0$	Reference density
$\zeta_0$	Reference geopotential height = 122.5 km
$g_0$	Reference gravitational acceleration
$k$	Boltzmann constant
$M(\zeta)$	Effective mass profile
$C, \zeta_C, H_C$	Chemical loss term parameters
$S_i(\zeta)$	B – spline basis functions
$\alpha_i$	Coefficients on B – splines
$N_S$	No. of basis functions = 10

Above 122.5 km geopotential height, the NO profile has the same formulation as the profile defined in Equation 2 of M2.0, transitioning to species-by-species hydrostatic equilibrium in the upper thermosphere via an effective mass profile. The NO profile includes a Chapman-like bottomside chemical loss term; a chemical/dynamical

correction term (with amplitude  $R$  in Equation 2 of M2.0) is also available but is not used for NO in MSIS 2.1. The piecewise-linear effective mass profile  $M(\zeta)$  follows Equation 5 of M2.0, which describes a monotonic transition (drawn through an asymmetric hyperbolic tangent function, with different scale heights for the upper and lower portions) from the mean molecular mass of the fully mixed atmosphere to the mass of an individual species. For NO, the effective mass profile parameter values are fixed a priori as follows (the values were chosen ad hoc to be similar to those of the  $N_2$  effective mass profile, except for the species molecular mass):

$$\begin{aligned} \bar{M} &= 28.96546 \text{ amu} && \text{Mass in fully mixed region (lower asymptote)} \\ M_s &= 30.0061 && \text{NO molecular mass (upper asymptote)} \\ \zeta_M &= 95 \text{ km} && \text{Transition, or "turbopause" height} \\ H_{ML} &= 6 \text{ km} && \text{Scale height of lower portion} \\ H_{MU} &= 17 \text{ km} && \text{Scale height of upper portion} \end{aligned} \quad (2)$$

The effective mass thus transitions from  $M = 28.97$  amu below 83 km ( $95 \text{ km} - 2 \times 6 \text{ km}$ ) to a constant 30 amu above 129 km ( $95 \text{ km} + 2 \times 17 \text{ km}$ ). The modeled NO profile is insensitive to these height parameters because the effective mass dependence has a direct effect only above the 122.5 km joining height and because the difference between the lower and upper asymptotes is relatively small ( $<4\%$ ).

Below 122.5 km, the NO profile consists of weighted cubic B-splines. The B-spline basis, illustrated in Figure 1b, extends from 70 to 122.5 km with uniform node spacing of 7.5 km. At the joining altitude of 122.5 km, the profile is constrained to be C1 continuous (continuous in the zeroth and first derivatives) so that the upper profile parameters determine the weights ( $\alpha_8, \alpha_9$ ) on the top two splines ( $S_8, S_9$ ).

The NO profile is thus defined by 12 parameters ( $n_0, C, \zeta_C, H_c, \alpha_0, \alpha_1, \dots, \alpha_7$ ), along with the temperature profile and the fixed effective mass profile. The influence of temperature extends down to 107.5 km via the C1 constraint;

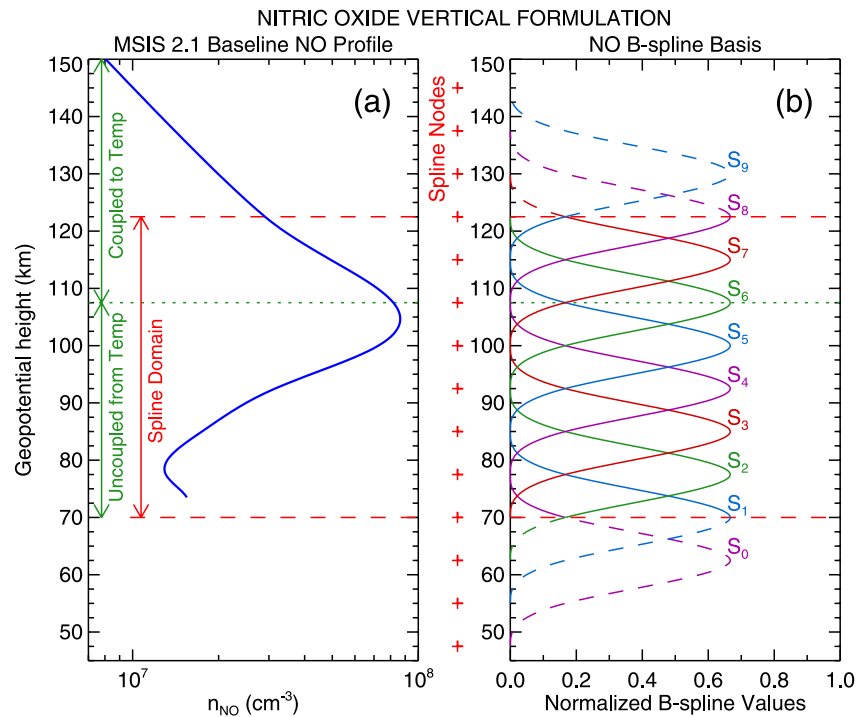


**Figure 1.** (a) MSIS 2.1 baseline (zeroth order) nitric oxide (NO) vertical profile (blue), as a function of geopotential height. The red dashed lines denote the 70–122.5 km domain of the B-spline basis used to represent the vertical profile. Above 122.5 km, NO is represented by a temperature-coupled Bates profile with height-dependent effective mass. C1 continuity is enforced at this joining point, so the influence of thermospheric temperature extends down to 107.5 km. (b) The individual normalized B-splines, with 7.5 km node spacing, that constitute the vertical profile basis.

below that altitude, the profile is decoupled from temperature. Figure 1a shows the baseline (spatiotemporally averaged at the reference solar and geomagnetic activity levels) MSIS 2.1 NO profile obtained as a result of the fitting process described in Section 4 and illustrates the spline region and the region coupled to temperature.

## 2.2. Expansion of Vertical Profile Parameters

As in MSIS 2.0, the vertical parameters are expanded as a function of spherical harmonics in latitude and local time or longitude; solar zenith angle (SZA); harmonics in day of year; polynomials of the  $F_{10.7}$  solar activity index (10.7 cm solar radio flux; Tapping (2013)); and a geomagnetic activity function. The full MSIS 2.0 expansion is given in Equations S15 and S16 of M2.0. For MSIS 2.1, five additional terms involving solar activity were added to the formulation:

Quadratic $\bar{F}_{10.7}$ term with cutoff, with latitude modulation $j = 310$	$+ \begin{cases} (\bar{F}_{10.7} - 150)^2 (\beta_j P_{0,0} + \beta_{j+1} P_{2,0} + \beta_{j+2} P_{4,0}) & ; \bar{F}_{10.7} \leq 150 \\ 0 & ; \bar{F}_{10.7} > 150 \end{cases}$
Latitude Modulation of $\Delta F_{10.7}$ $j = 313$	$+ (\bar{F}_{10.7} - \bar{F}_{10.7}) (\beta_j P_{2,0} + \beta_{j+1} P_{4,0})$

Definitions:

$j$	Starting index of term group (in the model code)
$F_{10.7}$	10.7 cm solar radio flux (at Earth) on previous day (sfu)
$\bar{F}_{10.7}$	Centered 81-day average of $F_{10.7}$
$\Delta F_{10.7}$	$F_{10.7} - \bar{F}_{10.7}$
$\beta_j$	Model parameters
$P_{n,m}$	$\frac{1}{2^n n!} \cos^m \phi_{gd} \frac{d^{n+m}}{dx^{n+m}} (x^2 - 1)^n ; x = \sin \phi_{gd}$ (Associated Legendre functions)
$\phi_{gd}$	Geodetic latitude

(3)

These new terms are needed to accurately capture the solar activity dependence evident in the data, as demonstrated in Section 5.4. For NO in MSIS 2.1, the quadratic term with a cutoff at  $\bar{F}_{10.7} = 150$  sfu (1 solar flux unit =  $10^{-22} \text{ W m}^{-2} \text{ Hz}^{-1}$ ) replaces the unlimited quadratic term used in MSIS 2.0 and earlier versions. With the new formulation, the  $\bar{F}_{10.7}$  dependence is purely linear for  $\bar{F}_{10.7} > 150$ , which provides a more robust extension of the model to high solar activity levels at which there is little or no data. The coupled  $\Delta F_{10.7}$ -latitude terms were added to confine the effects of short-term ( $\leq 27$  days) solar irradiance variations to low latitudes.

As with MSIS 2.0, some of the vertical parameters are not expanded beyond their global values (which we also refer to as the “baseline” or “zeroth order” terms) and some are expanded only sparsely. The specific expansion terms used for NO are described in Section 4.

## 3. Data

Table 1 summarizes the data sets and random samples we used to estimate the parameters of MSIS 2.1; acronym definitions are given at the end of the text. The fit assimilated only the first six data sets; a seventh data set, Envisat/SCIAMACHY, provided independent validation. We also used additional independent random samples of the fitting data sets for validation and analysis.

Brief descriptions of each data set are provided in Section 3.1. The generation of random samples for fitting and validation is described in Section 3.2. The full data sets and all of the data samples used for fitting and analysis are available in the repositories listed in the data availability statement.

**Table 1**  
*Summary of Nitric Oxide Data Sets and Samples Used to Estimate MSIS 2.1 Parameters<sup>a</sup>*

	Envisat/MIPAS	ACE/FTS	AIM/SOFIE	SNOE	Odin/SMR	UARS/HALOE	Envisat/SCIAM <sup>b</sup>
Measurement type	Infrared (5.3 $\mu$ )	Solar occultation	Solar occultation	UV scattering	Far infrared (552 GHz)	Solar occultation	UV scattering
Latitudes	86°S–88°N	85°S–86°N	82°S–89°N	80°S–80°N	89°S–89°N	79°S–78°N	83°S–83°N
Altitudes (km)	70–200	70–106	70–130	96–150	90–114	70–142	70–150
Years	2005–2012	2004–2020	2007–2020	1998–2003	2003–2020	1991–2005	2008–2012
No. unique days	334	5,342	3,852	1,987	1,180	3,337	110
No. unique profiles <sup>c</sup>	165,464	96,758	96,056	760,214	299,572	91,689	3,050
No. observations <sup>d</sup>	3,750,651	898,197	1,998,310	3,153,841	974,215	1,349,529	111,070
No. unique obs <sup>e</sup>	2,657,078	740,344	1,199,442	2,821,613	788,838	1,224,132	111,070
Fraction of full set <sup>f</sup> (%)	55	35	54	22	20	19	100
Data version	8	4.1	1.3	3	3	19	6.2
References	Funke et al. (2022)	Bernath (2017)	Hervig et al. (2019)	Barth et al. (2003)	Kiviranta et al. (2018)	Gordley et al. (1996)	Bender et al. (2013)

<sup>a</sup>Shown are statistics for all 15 fitting ensembles. <sup>b</sup>Envisat/SCIAMACHY data were not used in the fit. Shown are statistics of SCIAMACHY daily averages (in 5° latitude bins) used for independent validation. <sup>c</sup>Total number of unique profiles in the fitting ensembles. The random selection process operates at the observation level, so a given raw profile may not be fully sampled. <sup>d</sup>Total number of observations, randomly selected with repetition, in the fitting ensembles. <sup>e</sup>Number of unique observations in the fitting ensembles. <sup>f</sup>Number of unique observations divided by the number of observations in the full set (after applying the height, minimum density, and signal-to-noise criteria).

### 3.1. Data Sets

MIPAS was a limb-viewing midinfrared Fourier transform spectrometer on board Envisat, operating from 2002 to 2012. Temperature and abundances of many trace gases were measured globally from a sun-synchronous orbit with descending and ascending nodes at approximately 1000 and 2200 local time, respectively (Fischer et al., 2008). While nominal observations covered the vertical range 5–70 km, dedicated upper atmosphere observations were performed less frequently (about 1 day out of 10) during 2005–2012. We used Version 8, Level 2 joint temperature-NO retrievals (Funke et al., 2022) from the upper atmosphere observation mode. NO is provided in the files as volume mixing ratio (VMR; e.g., Houghton, 1986, p. 20); we converted VMR to number density by multiplying by the total number density calculated from the provided pressure and retrieved temperature. We excluded observations for which the quality field “AKM\_diagonal” was less than 0.03.

ACE is a small science satellite (Bernath, 2017) that carries a high-resolution infrared Fourier transform spectrometer operating in solar occultation mode. We used Version 4.1 retrievals (Boone et al., 2020) in which NO was retrieved (i.e., excluding scaled a priori values). NO is retrieved in the 8–107 km altitude range at the poles and 10–107 km at the equator. NO is provided as VMR; we converted to number density by multiplying by the total number density calculated from the provided pressure and retrieved temperature.

SOFIE, onboard the AIM satellite, uses solar occultation and differential broadband radiometry and has measured NO from May 2007 to present. Gómez-Ramírez et al. (2013) provide a detailed description of the NO measurements, signal corrections, and retrievals. Hervig et al. (2019) report a validation of the V1.3 NO results including comparisons with ACE and MIPAS. These comparisons indicate mean differences of less than ~50% for altitudes from roughly 50 to 100 km for SOFIE spacecraft sunrise and from 50 to 140 km for SOFIE sunsets. The recommended SOFIE NO results have been filtered for polar mesospheric cloud (PMC) contamination and vertically smoothed in post processing to the effective resolution of ~3 km (Hervig et al., 2019). In this study, we used this V1.3 mission file, which reports NO number density.

SMR is a limb emission sounder on board Odin, which is a Swedish-led research satellite launched in 2001 into a sun-synchronous orbit with a ~1800 local time ascending node. SMR measures globally a variety of trace gases as well as temperature in the middle atmosphere. NO is retrieved from the observation of two thermal emission



lines in a band centered near 551.7 GHz. The retrievals cover altitudes from  $\sim 45$  to 115 km during both day and night, with nearly global latitude/longitude coverage. The vertical resolution ranges from 3 to 4 km in the upper stratosphere to 10 km in the upper mesosphere and lower thermosphere. The NO observational program started in October 2003 and is still ongoing, making this data set one of the longest NO concentration records available in the considered altitude region. The temporal sampling has changed throughout the mission: NO was measured 1 day per month before 2007 and 4–5 days per month after this date. It is occasionally measured much more frequently during dedicated observational campaigns, which can be scheduled in order to carry out specific case studies (P  rot & Orsolini, 2021). We used Version 3 NO retrievals. Although no rigorous validation study has yet been performed for this latest data version, the study by Kiviranta et al. (2018) constituted an indirect comparison between Odin/SMR and four other data sets. They showed that SMR was in good agreement with other instruments in a limited altitude range (85–115 km). NO is provided as VMR; we converted to number density by multiplying by the total number density calculated from the provided a priori background pressure and temperature.

HALOE conducted solar occultation measurements from UARS from 1991 to 2015. HALOE measured NO using gas correlation, where the light passing through a cell containing NO was compared with that passing through a vacuum. This approach removes interference from aerosols and spectrally overlapping trace gases. The HALOE NO measurements, retrievals, and validation are described by Gordley et al. (1996) and McHugh et al. (2005). Compared to ACE, HALOE NO was within  $\sim 20\%$  below 60 km and  $\sim 50\%$  higher above  $\sim 90$  km (McHugh et al., 2005). We used Version 19 NO retrievals. NO is provided as VMR; we converted to number density by multiplying by the total number density calculated from the pressure and temperature.

SNOE measured NO from 1998 through 2003 by observing limb scattered sunlight at 215 and 237 nm. A polar orbit allowed observations from  $80^\circ\text{S}$  to  $80^\circ\text{N}$  at 15 longitudes per day. For the northern summer of 2000 and southern summer of 2000/2001, a special mode of operations focusing on PMCs prohibited observations at tropical latitudes (Bailey et al., 2007). We used Version 3 retrievals, which are published here for the first time and which extend the data set presented by Barth et al. (2003) an additional 3 years, out to the end of the mission in late 2003. A netCDF file containing this new version is available at the repository listed in the data availability statement; NO is provided as number density. This extended data set uses emission rate factors of NO at the SNOE wavelengths calculated by Stevens (1995). This change is discussed in Barth and Bailey (2004) and yields an approximately 14% increase in the magnitude of NO relative to the 1998–2000 SNOE data set described by Barth et al. (2003). We note that NOEM is based on the 1998–2000 Barth et al. (2003) data set but adjusted to be consistent with the Stevens (1995) emission rate factors, so that the scaling of the data used in NOEM (Marsh et al., 2004) is consistent with the SNOE data used in this study.

Envisat/SCIAMACHY NO densities were derived from the fluorescent emissions in the NO gamma bands (e.g., Cleary et al., 1995), measured using mesosphere-lower thermosphere scans (MLT, 50–150 km). These scans were carried out every 15 days from July 2008 until April 2012. The retrieval algorithm utilizes slant column inversion on a 2-dimensional orbit-wise grid with an altitude spacing of 2 km from 60 to 160 km and a latitude spacing of  $2.5^\circ$  from  $90^\circ\text{S}$  to  $90^\circ\text{N}$  (Bender et al., 2013). The emission rate factor calculations used in the retrievals are consistent with those of Stevens (1995) to within a few percent (Bender et al., 2013, Table 2); therefore, the scaling of the SCIAMACHY data should be approximately consistent with that of SNOE.

We used SCIAMACHY Version 6.2 NO MLT mode retrievals for independent validation and analysis only; these data were not used in MSIS 2.1 parameter estimation. NO is provided as number density. Following Bender et al. (2015), we computed daily average profiles of the NO density in  $5^\circ$  latitude bins, which is equivalent to daily zonal means from at most 15–16 sampled longitudes. We required a minimum of 6 observations to make an average, and we excluded records for which (a) the resulting average diagonal element of the averaging kernel matrix was less than 0.02, (b) the average SZA was greater than  $90^\circ$ , or (c) the average density was less than or equal to zero. After application of the first two criteria, the positive definite criterion (which is necessary for analysis in log space) eliminated 8.2% of the remaining zonal mean values. The rightmost column of Table 1 summarizes the spatiotemporal coverage and statistics of the resulting reduced data set, which we used in the analyses presented in Section 5.

### 3.2. Sampling Procedure and Distributions

From the NO data sets described in Section 3.1, excluding SCIAMACHY, we assembled 30 random samples, which we call ensembles. We used the first 15 ensembles for fitting via sequential estimation and the second 15 for validation.

In creating the ensembles, we only considered observations between 70 and 200 km geometric altitude, NO density values greater than  $100 \text{ cm}^{-3}$ , and measurements with signal-to-noise ratios (measurement value divided by uncertainty) greater than 0.5. This last criterion was only applied to MIPAS, ACE, SMR, and HALOE, for which measurement uncertainties were provided in the data files.

The size of each ensemble is  $\sim 905,000$  observations. The relative sizes of the samples from each instrument were chosen subjectively, in order to obtain a balance among instruments and measurement types, including consideration of the differing altitude grids of the data sets. Table 1 summarizes the spatiotemporal coverage and sampling statistics of the fitting ensembles (ensembles 1–15). Figure 2a shows the distribution of the data in the fitting ensembles as a function of altitude in 5 km bins. The distributions represent the weight of each data set's contribution to the model; in the fitting process, each of the sample observations is weighted equally.

The random selection process did not exclude duplicates, so some observations will appear more than once in a given ensemble, or across ensembles. For large data sets the statistical influence of duplicates is negligible. For small data sets the duplicates increase the influence of underrepresented measurement techniques. The total number of fitted observations for each data set is listed in Table 1, along with the number of unique observations and the fraction of the full data set (after applying the height, minimum density, and signal-to-noise criteria) that this number represents. Also listed are the number of unique vertical profiles represented in the fitting ensembles. All six data sets consist of vertical scans of short temporal duration; the random sampling is applied to the individual observations, not the profiles. Table 1 also includes the number of unique days (i.e., unique 24-hr Universal Time periods) represented in the sample.

In the 97–150 km altitude range, SNOE has the greatest representation in the fitting ensemble. However, MIPAS has the greatest representation overall (3.8 million observations vs. 3.2 million for SNOE) as a result of its broader altitude coverage. Near the NO density peak ( $\sim 105 \text{ km}$ ), all six data sets have approximately equal representation.

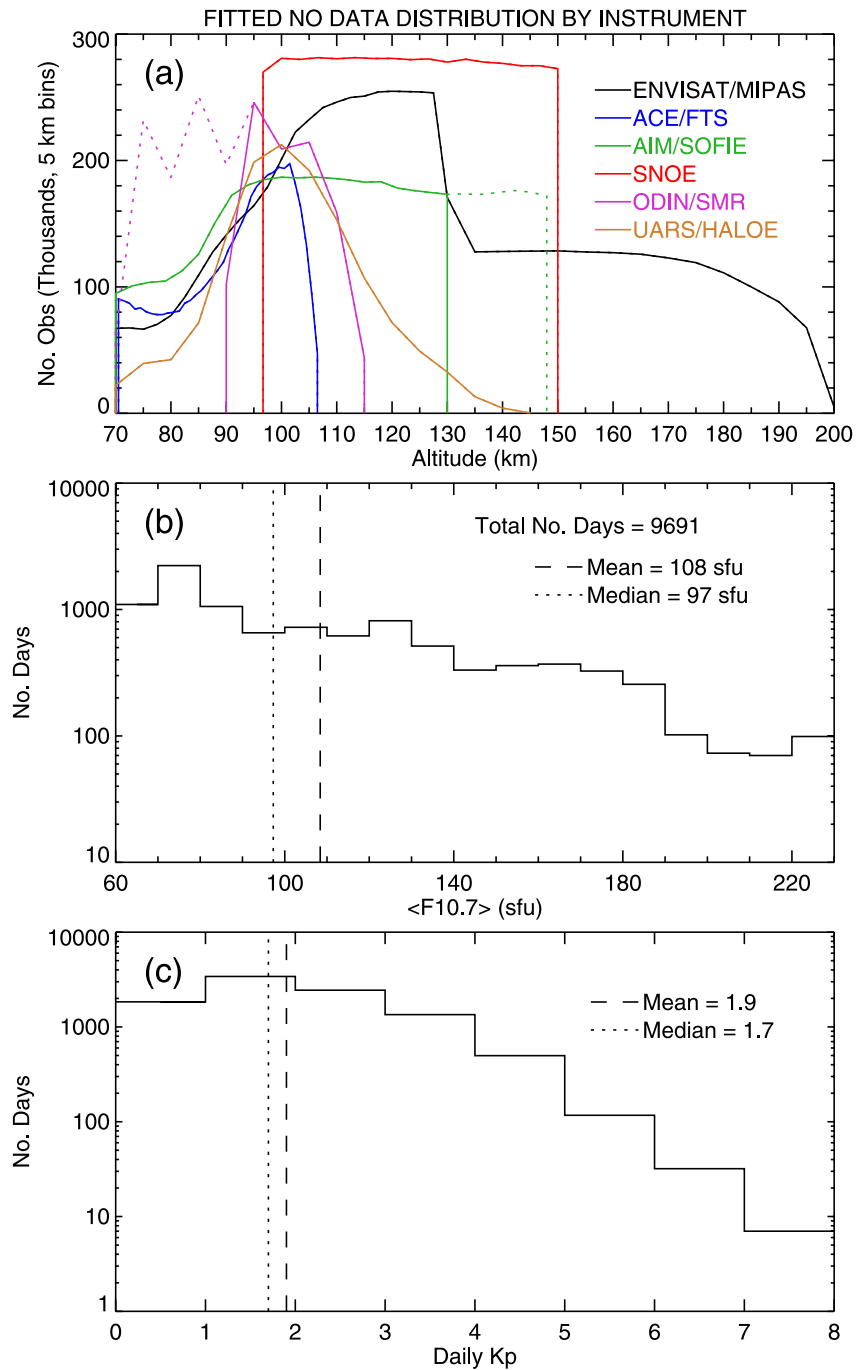
After generating the ensembles, we further excluded SOFIE data above 130 km and SMR data below 90 km from the fitting process. As shown in Section 5, there are large systematic differences in these respective altitude regions relative to the other data sets, which motivated the exclusions. We retained these data for the analyses presented below; the full altitude distributions of the SOFIE and SMR data are shown by the dotted lines in Figure 2a.

Figure 2b shows the distribution of the fitting ensembles (combining all data sets) as a function of solar activity, as represented by the 81-day average  $F_{10.7}$  index,  $\bar{F}_{10.7}$ . The bulk of the observations were taken after 2003, which includes only a weak solar maximum of  $\bar{F}_{10.7} \cong 160 \text{ sfu}$  in 2014, so the average  $\bar{F}_{10.7}$  of the ensembles (weighted by unique days) is only 108 sfu. However, the SNOE and HALOE data sets include observations during the stronger solar maxima in the early 2000s and 1990s, and there are  $\sim 300$  days in the sample for which  $\bar{F}_{10.7} > 200 \text{ sfu}$ .

Figure 2c shows the distribution as a function of geomagnetic activity, as represented by the daily average  $Kp$  index ( $Kp_{\text{daily}}$ ). The number of observations falls off exponentially with increasing  $Kp$  but there are  $\sim 30$  days for which  $6 \leq Kp_{\text{daily}} < 7$  and 7 days for which  $Kp_{\text{daily}} \geq 7$  (the maximum value is 7.7).

Figure 3 further illustrates the distribution of the fitting ensembles as a function of local time, latitude, and day of year. One important characteristic of currently available NO data sets is that the local time coverage at mid and low latitudes is limited (Figure 3a; local time coverage is less relevant at high latitudes where the seasonal insolation cycle dominates over the diurnal cycle). Envisat and SNOE were, and Odin is, in sun-synchronous orbits, while the solar occultation instruments only sample near the terminator. The limited local time coverage of the individual data sets makes it very difficult to distinguish true local time effects from mutual biases among the data sets. As the SNOE orbit decayed, it began to precess toward later local times (1200–1600) during 2001–2003 but this drift coincides with decreasing solar activity.





**Figure 2.** (a) Geodetic altitude distribution of nitric oxide data assimilated into MSIS 2.1. The solid lines show the number of fitted observations from each instrument (color coded as indicated in the legend) in 5 km bins, summed over all 15 fitting ensembles. The dotted lines show the coverage of additional data from Odin/SMR and AIM/SOFIE that were used in the postfit model analysis but not in the fitting of the model. (b) Distribution of the number of unique Universal Time days (log scale) in the fitting ensembles (combining all instruments), as a function of the 81-day average  $F_{10.7}$  in 10 sfu bins. The dashed and dotted lines, respectively, mark the mean and median of the distribution. The total number of unique days is 9,691. Panel (c) same as panel (b), but as a function of the daily  $K_p$  geomagnetic activity index.

Figure 3b shows that the seasonal-latitudinal distribution is fairly uniform overall, even though the sampling patterns of the solar occultation instruments are somewhat discrete. Therefore, we do not expect any significant aliasing issues to occur in our estimation of the seasonal-latitudinal parameters of the model.

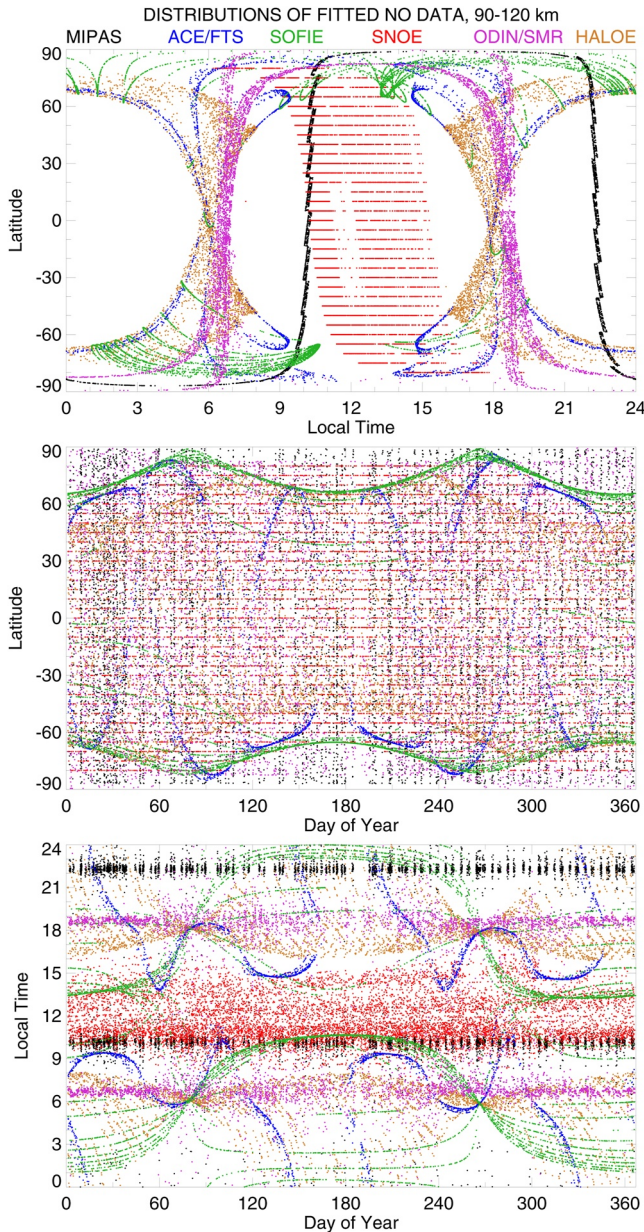


**Figure 3.** Distribution of nitric oxide data assimilated into MSIS 2.1 as a function of (top) latitude and local time, (middle) latitude and day of year, and (bottom) local time and day of year. Shown is a 10% random sample of a single fitting ensemble, further restricted to altitudes between 90 and 120 km. Data from each instrument are color coded as indicated in the legend.

## 4. Model Parameter Estimation Procedure

In this section we describe the procedure used to set or estimate the MSIS 2.1 NO parameters; the parameters for the other species and temperature are unchanged from MSIS 2.0. For some NO parameters, we assigned constant, a priori values, but we tuned most parameters to the fitting ensembles described in Section 3.2. The final parameter values are tabulated in Data Set S1, which can be referenced to determine which variations in NO are active in the model. The units of the reference log density and spline coefficients ( $\ln(n_0)$  and  $\alpha_i$  in Equation 1) are  $\ln(\text{m}^{-3})$ . A total of 299 nonzero parameters describe NO in the MSIS 2.1 mesosphere and thermosphere, together with the parameters that specify the temperature, to which the MSIS NO density is directly coupled above 107.5 km geopotential height.

### 4.1. Fixed a Priori Parameters

For several of the NO model parameters, we set the values a priori without further tuning. First, as discussed in Section 2.1, the NO effective mass parameters are set to the values given in Equation 2 and are not expanded beyond those global values. Second, the reference height  $\zeta_C$  of the Chapman-like chemical loss term was fixed at 122.5 km. Third, the geomagnetic activity dependence incorporates linear and exponential terms in the  $ap$  index (Hedin, 1987, Equations A23 and A24d; M2.0, Equation S16), described by parameters  $k_{00}^r$  and  $k_{00}^s$ , respectively, in Hedin's notation. Based on our finding that the geomagnetic activity effect saturates at moderate geomagnetic activity levels (see Section 5.5), we fixed the coefficient of the linear term at zero; the parameter in the exponential term was tuned as part of the fitting process described in Section 4.3. Fourth, the storm-time mode of geomagnetic activity dependence, which is a function of the time history of the 3-hr  $ap$  index, includes a parameter  $\beta_{00}$  that describes how fast the weighting of the  $ap$  index decreases exponentially with increasing lag (Hedin, 1987, Equation A24). We fixed the value of  $\beta_{00}$  for all of the NO vertical profile terms at  $2.62 \times 10^{-5} \text{ s}^{-1}$ , which is the same value used for atomic oxygen in MSIS 2.0 and MSISE-00 and is similar to the values used for other species; the model performance is not sensitive to the choice of value.

### 4.2. Initialization of Tuned Parameters

Prior to fitting, we initialized the NO global vertical profile parameters (other than the ones already fixed a priori as described in Section 4.1) to values that produce a rough approximation of the observed profile:

$$\begin{aligned} (n_0)_{\text{init}} &= 2.905 \times 10^{13} \text{ m}^{-3} \\ (C)_{\text{init}} &= 1 \\ (H_C)_{\text{init}} &= 20 \text{ km} \\ (\alpha_i)_{\text{init}} &= 31 = \ln(2.905 \times 10^{13}) ; i = 0, 1, \dots, 7 \end{aligned} \quad (4)$$

We then conducted a preliminary fit using geomagnetically quiet NO density output from the NOEM empirical model (Marsh et al., 2004) and the NCAR TIME-GCM physics-based model (Roble, 1996; Roble & Ridley, 1994). The set of NOEM values was produced by evaluating the model for  $Kp = 1.0$ , on the 15th of each month, and for  $F_{10.7} = 70, 100, 130, 160$ , and 200 sfu. The NOEM grid covers altitudes from 100 to 150 km at 3.33 km intervals and magnetic latitudes from 80°S to 80°N at 5° intervals. The TIME-GCM values are from the experiments described by Jones et al. (2014). We used output from steady state, diurnally reproducible

(e.g., Killeen & Roble, 1986) runs on the 15th day of each month, with  $F_{10.7} = 70, 110$ , and  $200$  sfu. All of the TIME-GCM experiments used a geomagnetic activity level of  $Kp \cong 1.0$ . We first tuned the model parameters, including selected expansion terms, to the TIME-GCM output via unweighted, Levenberg-Marquardt chi-square minimization (using ODRPACK95; Zwolak et al., 2007). We then further tuned the upper vertical parameters (the coefficients  $\alpha_6, \alpha_7$  on the top two splines and  $n_0, C, H_c$ ) and their expansions to the NOEM output.

The preliminary parameter values are summarized in Data Set S2. With the exception of one group of terms (described below), the parameters that we initially tuned to TIME-GCM and NOEM are a subset of the final parameters estimated as described in Section 4.3 using the data ensembles and were overwritten by that least squares fit.

However, one group of terms was carried over from the TIME-GCM fit to the final fit without further tuning. We included a hyperbolic tangent function of the SZA (to capture day-night photochemical effects) in the expansion of  $n_0, C, \beta_6$ , and  $\beta_7$ . An  $\bar{F}_{10.7}$  modulation of this term was additionally applied to  $n_0$  and  $C$ . Because of the poor local time coverage of the existing NO data sets, as shown in Figure 3, we did not attempt to tune the SZA parameters to the data ensembles (or to NOEM, which is based on SNOE and does not include a local time variation). This variation of the model, which is relatively small, is therefore derived solely from TIME-GCM. Above 107.5 km, the local time variation of MSIS 2.1 NO is dominated by its coupling with the MSIS 2.0 temperature, which has its own local time variation. The local time dependence of the MSIS 2.1 NO model and the underlying data are discussed in Section 5.6.

### 4.3. Sequential Fitting of Parameters

Starting with the preliminary parameter set derived from TIME-GCM and NOEM output, as described in Section 4.2, we tuned the NO model to the data ensembles. We separately assimilated each of the first 15 ensembles in sequence, using the parameter set from one ensemble as the starting estimate for the next ensemble. For each ensemble, we tuned different groups of parameters in the stages outlined below, similarly using the parameter set from one stage as the starting state for the next stage. In each fitting stage the global values of  $n_0, C, H_c, \alpha_0, \alpha_1, \dots, \alpha_7$  were retuned, in order to prevent aliasing of the expansion terms into the baseline profile (cf., Picone, 2008). We conducted all parameter estimation stages via unweighted, Levenberg-Marquardt chi-square minimization (using ODRPACK95; Zwolak et al., 2007).

In the first stage of tuning for each ensemble, we estimated the global parameters and the coefficients of their latitudinal expansion (Legendre functions up to degree 6); these parameters are denoted “time-independent” in Data Set S1. The coefficients on the lowest four B-splines ( $S_0$ – $S_3$ ) were computed up to degree 4, while the coefficients on top four splines ( $S_4$ – $S_7$ ) and  $n_0, C$  were computed up to degree 6.

In the second stage, we fitted annual harmonics coupled with the Legendre function expansion in latitude; these parameters are denoted “Annual” in Data Set S1. The annual harmonic coefficients (sine and cosine) on  $n_0, C$ , and the top two splines ( $S_6$  and  $S_7$ ) were computed up to degree 5 in latitude and the bottom six splines ( $S_0$ – $S_5$ ) up to degree 3.

In the next fitting stage, we estimated the solar activity parameters; these parameters are denoted “Solar Activity” or “Other” in Data Set S1. The linear and quadratic terms in  $\bar{F}_{10.7}$  were applied to  $n_0, C$ , and all of the splines (the definitions and notation of the  $\bar{F}_{10.7}$  terms are given in Equation 3). As described in Section 2.2, the quadratic term is deactivated for  $\bar{F}_{10.7} > 150$  sfu.  $P_{2,0}$  and  $P_{4,0}$  latitudinal modulations of the  $\bar{F}_{10.7}$  linear and quadratic terms were included in the fit of  $n_0, C$ , and the top five splines. The  $\Delta F_{10.7}$  term and  $P_{2,0}$  latitudinal modulation thereof were applied to  $n_0, C$ , and the top four splines. Due to the limited amount of NO data for very high  $\bar{F}_{10.7}$  conditions (Figure 2b), we doubled the weight of HALOE and SNOE observations for  $\bar{F}_{10.7} \geq 200$  to ensure robust fitting and model behavior at such high but relatively rare solar activity conditions.

In the final two fitting stages, we fitted the geomagnetic activity parameters, tuning the parameters for the daily  $Ap$  mode and the storm-time  $ap$  history mode in separate stages. These parameters are denoted “Geomagnetic Activity (daily)” and “Geomagnetic Activity (3 hr)” in Data Set S1. Only one (at most) of these two groups of parameters is active in the model, depending on the model switch settings, so the estimates are independent of each other. The  $P_{0,0}$  and  $P_{2,0}$  geomagnetic activity terms were applied to  $n_0, C$ , and the top five splines; the  $ap$

exponential relaxation rate parameter  $k_{00}^s$  (see Section 4.1) was also tuned for each these vertical parameters. The  $P_{4,0}$  geomagnetic activity term was applied to  $n_0$ ,  $C$ , and the top three splines.

For the final parameter estimates, we computed the average of the parameters derived from ensembles 6–15, omitting the results from the first five “spin-up” ensembles. The final parameter values are given in Data Set S1.

Although the vertical B-spline basis and fitted data extend down to 70 km geopotential height, we analyze model output only above 72.5 km, and the model code included in Supporting Information S2 or S3 supplies missing values at heights below 72.5 km. This cutoff height is motivated by an artifact in the fitted baseline (zeroth order) profile, which contains an unrealistic local density maximum near 72 km (NO density should continue to increase with decreasing altitude in this region). This artifact does not occur when the model is evaluated for specific seasonal-latitudinal conditions, so it does not imply a problem with the model's representation of the data. The proximity of the artifact to the lower boundary of the spline domain, which is also the lower limit of our fitted data, may be a contributing factor. In future development, the effect could be corrected by extending the database and the spline domain downward and/or imposing boundary constraints on the second derivative of the model profile.

## 5. Validation and Science Results

In this section, we examine the structure of the MSIS 2.1 NO density and compare it with binned averages of the validation ensembles (see Section 2.3) and data-minus-model residuals thereof. We consider each of the model's input variables in turn and demonstrate that the model accurately represents the average behavior of the data (with a few exceptions) to within the variance of analysis results from the different data sets.

The data sets of NO number density, denoted here by  $n$ , follow an approximately lognormal distribution, as is often the case for positive definite quantities. That is, the distribution of  $\ln n$ , the natural logarithm of NO density, is approximately normal, consistent with our least squares fitting procedure for evaluating the MSIS model parameters.

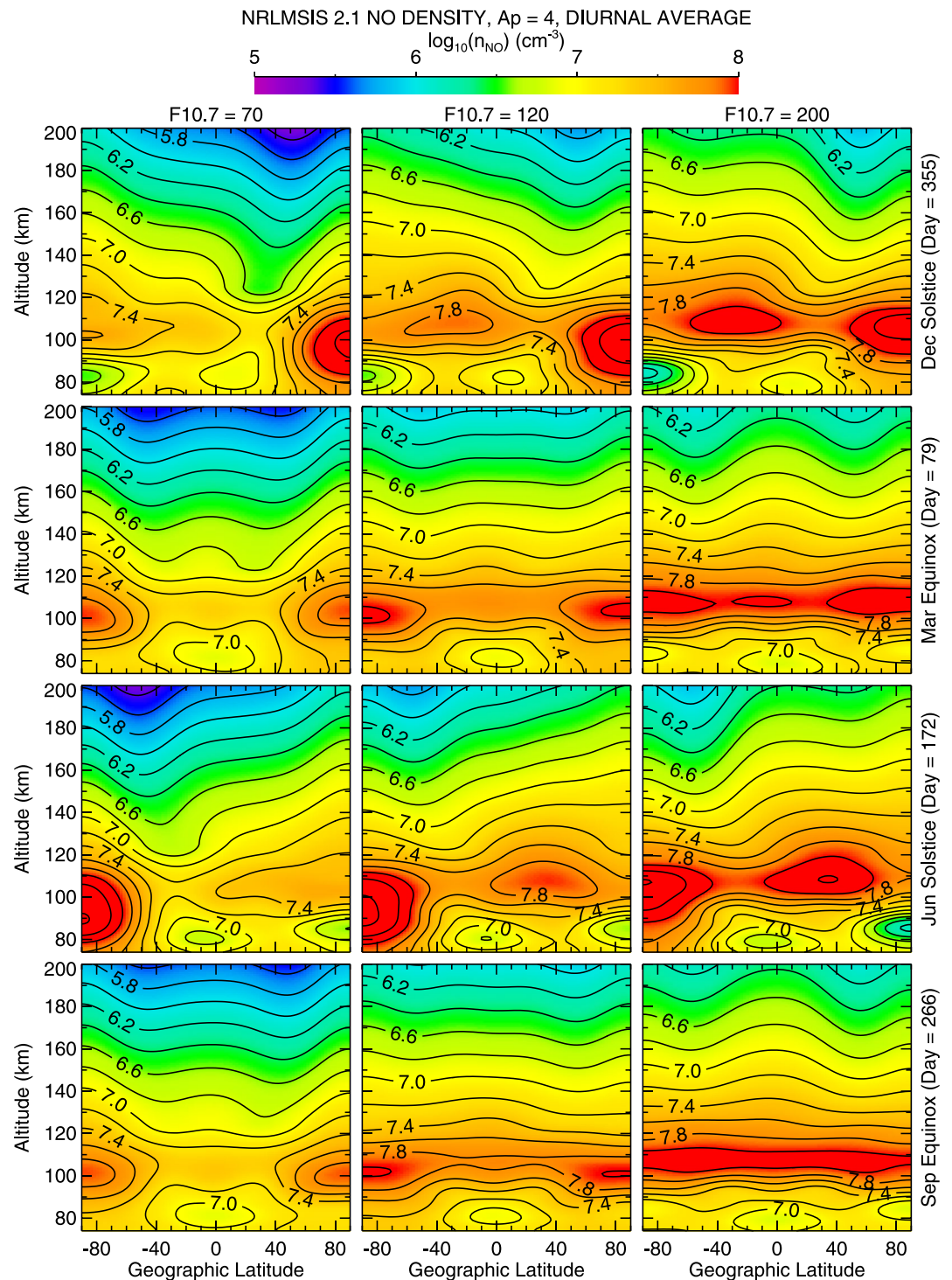
For this reason, and following the approaches used for MSISE-00 (Picone et al., 2002) and MSIS 2.0, we analyze the logarithmic data set  $\{d_i \equiv \ln n_i, i \text{ ranging}\}$  and the corresponding set of MSIS values,  $\{m_i \equiv \ln n_{i(\text{MSIS})}, i \text{ ranging}\}$ , in terms of (a) the model bias (mean of the data-minus-model residuals), denoted by  $b$  and (b) the standard deviation  $\sigma$  of the data about the bias-adjusted model. Note that for the logarithmic data set and denoting a mean over data by angle brackets, the model bias is  $b = \langle d_i - m_i \rangle = \langle \ln n_i / n_{i(\text{MSIS})} \rangle$ . Accounting for model bias, the standard deviation of the data about the model is then  $\sigma = [\langle (d_i - m_i)^2 \rangle - b^2]^{1/2} = [\langle (\ln n_i / n_{i(\text{MSIS})})^2 \rangle - b^2]^{1/2}$ . For reference, a difference of 0.1 in natural log space (e.g.,  $\ln(\text{data}/\text{model})$ ) corresponds to a  $\sim 10\%$  difference in number density; a difference of 0.7 in log-density space corresponds to approximately a factor of 2 difference in number density.

Tables S1 and S2 in Supporting Information S1 contain the bias and standard deviation performance statistics for the model. We computed these metrics for each data set and in selected altitude bins. We point out that the bias indicates systematic differences between a data set and the corresponding model estimates, while the standard deviation indicates the agreement between the geophysical variations in the data and model (it also includes measurement noise and accounts for the computed model bias).

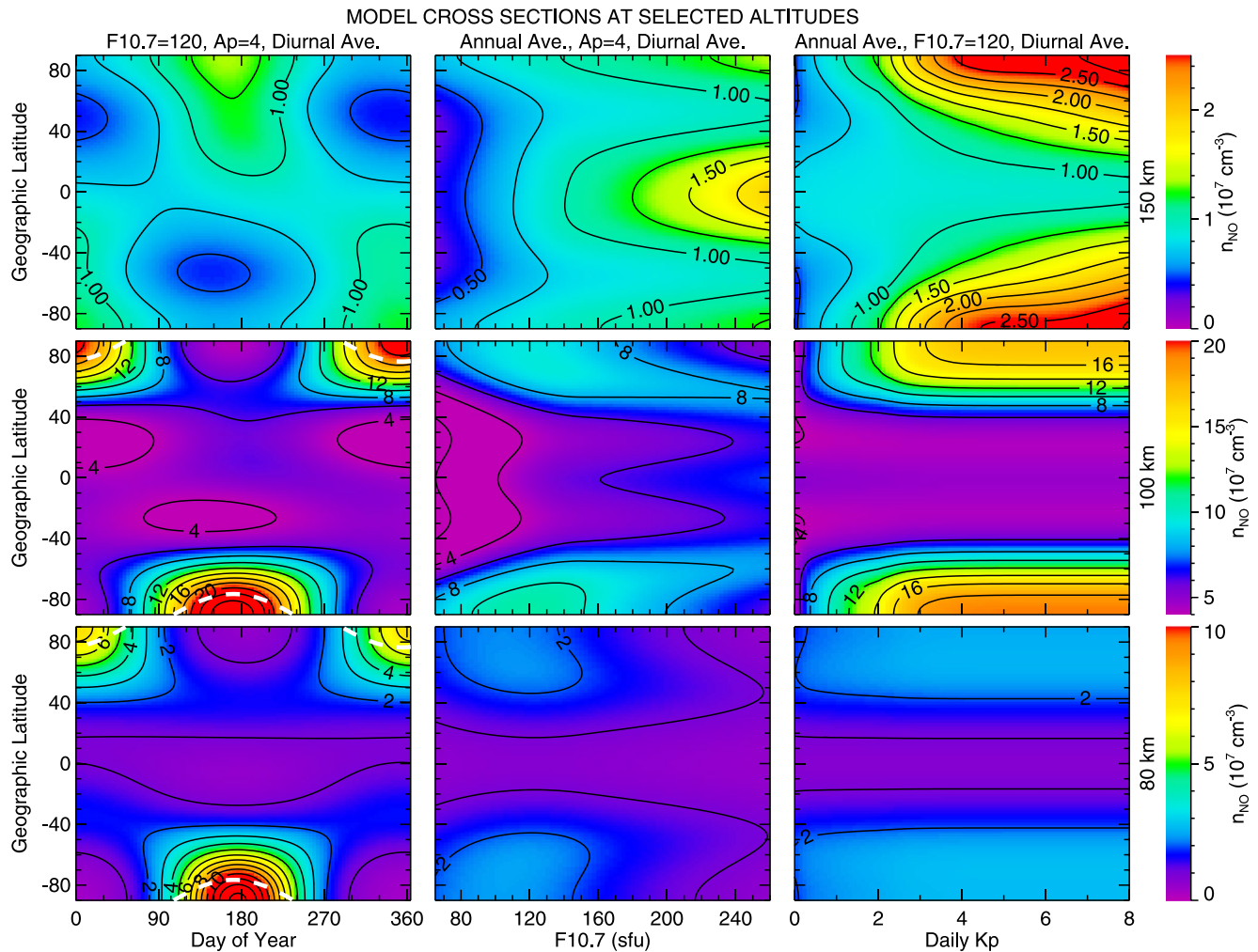
### 5.1. Model Cross Sections

Figure 4 shows height-latitude contours of the MSIS 2.1 NO log density, at the solstices and equinoxes and for solar minimum, moderate, and maximum conditions. The most prominent feature is an overall peak at winter solstice high latitudes, with model densities as high as  $2.5 \times 10^8 \text{ cm}^{-3}$  (8.4 in  $\log_{10}$  space). This maximum is due to the lack of photolytic loss in the polar night region. At winter latitudes above  $\sim 40^\circ$  and solar minimum and moderate conditions, the NO density profile forms a broad peak around 90–95 km. Under solar maximum conditions, this peak erodes somewhat on the bottomside and moves up to 100–105 km.





**Figure 4.** MSIS 2.1 nitric oxide (NO)  $\log_{10}$ -density as a function of altitude (74–200 km) and latitude (90°S–90°N). Results are shown in different rows for the solstice and equinox conditions indicated at the right and for solar minimum (left,  $\overline{F}_{10.7} = 70$  sfu), moderate (center,  $\overline{F}_{10.7} = 120$  sfu), and maximum (right,  $\overline{F}_{10.7} = 200$  sfu) conditions. In all cases, the results are diurnally averaged at quiet geomagnetic activity ( $A_p = 4$ ). The contour interval is 0.2 (~58% increase with each successively higher contour).



**Figure 5.** (Left) MSIS 2.1 nitric oxide (NO) density as a function of latitude and day of year, for solar moderate ( $\bar{F}_{10.7} = 120$  sfu) and geomagnetically quiet ( $A_p = 4$ ) conditions. In the lower two panels, the dashed white line marks the approximate solar terminator (solar zenith angle =  $100^\circ$ ) at noon, which is the boundary of the polar night region. (Center) Same, but as a function of latitude and  $\bar{F}_{10.7}$ , for annually averaged, geomagnetically quiet ( $A_p = 4$ ) conditions. (Right) Same, but as a function of latitude and daily  $K_p$  for annually averaged, solar moderate ( $\bar{F}_{10.7} = 120$  sfu) conditions. Results are shown at three altitudes: (Top) 150 km, (middle) 100 km, and (bottom) 80 km. In all cases, the results are diurnal averages. The contour intervals and color range are different for each altitude, as indicated by the contour labels and color scales to the right.

The summer hemisphere peak density occurs at 105–110 km and is narrower in altitude than the winter peak. At solar minimum, the largest summer densities are near the pole but for solar moderate and maximum conditions, they occur at midlatitudes. At solar maximum, the summer midlatitude density is comparable to the winter high-latitude density.

At the equinoxes, the density peaks at about the same altitude at all latitudes:  $\sim 100$  km at solar minimum, increasing to  $\sim 110$  km at solar maximum. At solar minimum, the density is concentrated at high latitudes. At solar maximum, the density is fairly evenly distributed with latitude.

Figure 5 shows additional cross sections of the model at three selected altitudes (80, 100, and 150 km); note that these plots show number density (different scales for each altitude) not log density. The left panels show latitude-season cross sections. At 80 and 100 km, the density is strongly concentrated in the polar night regions, which are delimited by the white dashed lines. The density in these regions is larger in the Southern Hemisphere than in the Northern Hemisphere, particularly at 80 km. At 150 km, the largest densities occur in the summer, not winter. At this altitude, the model NO density is strongly coupled to temperature (Equation 1); the higher summer



temperature expands the atmospheric column and produces larger densities at fixed altitudes. In the real atmosphere, NO density above 150 km is coupled to O<sub>2</sub>, as discussed in Section 7, and O<sub>2</sub> is coupled to temperature.

The center panels of Figure 5 show latitude- $\bar{F}_{10.7}$  cross sections of the model. At 80 km and 100 km, the  $\bar{F}_{10.7}$  dependence is weak compared to the seasonal dependence. At high latitudes, the model density at these altitudes has a weak maximum at  $\bar{F}_{10.7} = 100\text{--}110$  sfu and decreases slightly with increasing  $\bar{F}_{10.7}$  at higher solar activity levels. At low and midlatitudes, the density increases monotonically with increasing  $\bar{F}_{10.7}$ . At 150 km, the density increases with  $\bar{F}_{10.7}$  at all latitudes and solar activity levels, most strongly at low latitudes.

The right panels of Figure 5 show latitude- $Kp$  cross sections. At 80 km, the geomagnetic activity dependence of the model is very weak. At 100 km, the effect is concentrated at latitudes above 40°; it increases rapidly up to daily average  $Kp \sim 3$  and then levels off. At 150 km, the effect extends to lower latitudes and does not saturate as strongly, as a result of coupling with the geomagnetic activity dependence of the model temperature.

In the following subsections, we examine the major model features described above in more detail and compare directly with the underlying measurements.

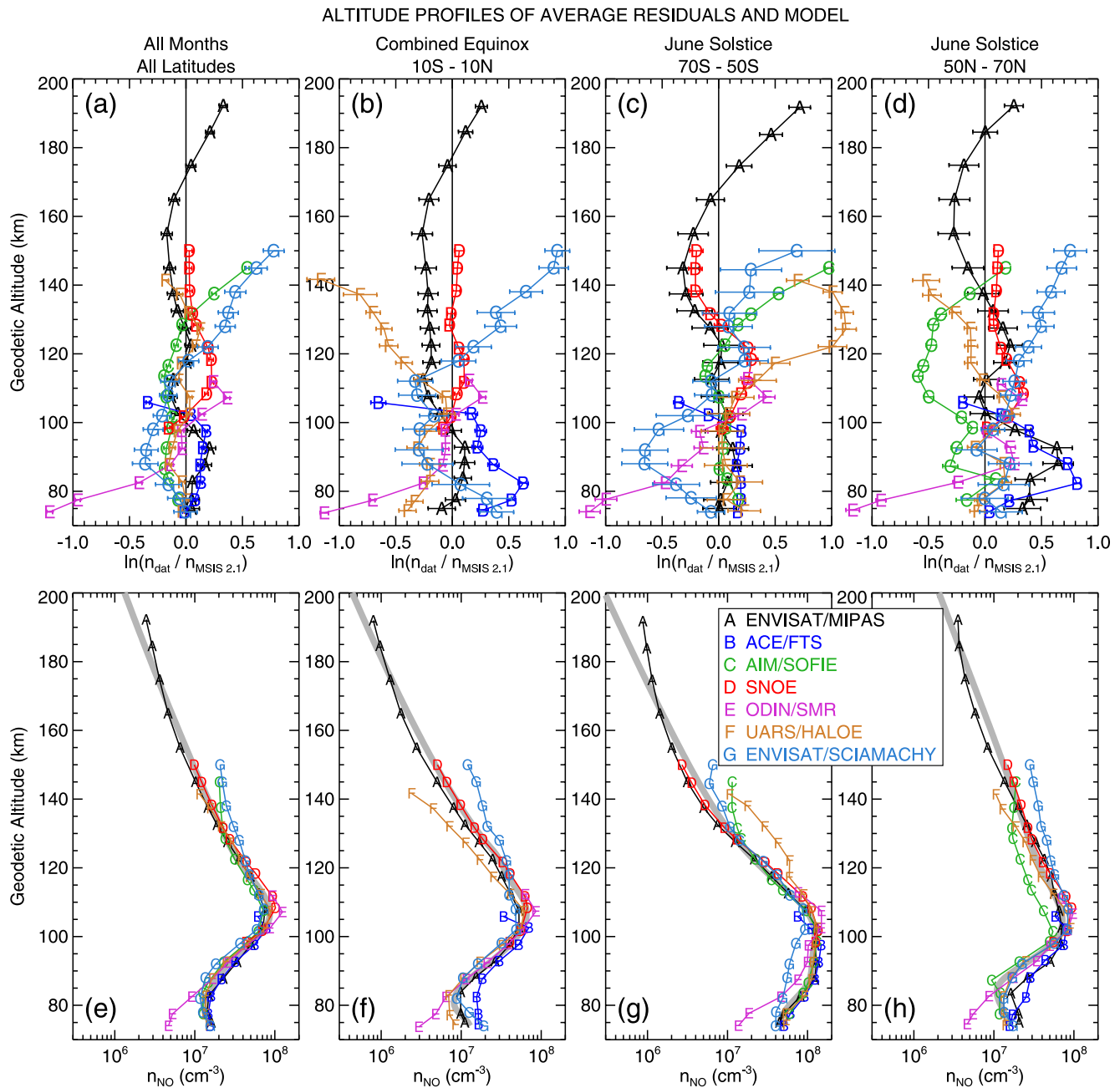
## 5.2. Altitude Dependence

Figure 6a shows height profiles of bin-average residuals computed using the validation ensembles, as well as the SCIAMACHY daily averages, as a function of altitude. These results are for geomagnetically quiet conditions but combine data from all seasons, latitudes, and solar activity. The average deviations of the data sets from the model are typically  $\pm 0.2$  in natural log space or about 22%. None of the data sets exhibits an offset that is uniform with altitude; each data set has positive offsets at some altitudes and negative offsets at others, with patterns that are largely unique. This suggests that the offsets to a large extent originate among the data sets, and that the model accurately represents the collective altitude dependence of the data. For example, the average SNOE deviations from the model are slightly negative below 105 km, positive (up to  $\sim 0.2$ ) between 105 and 125 km, and near zero from 125 to 145 km. In contrast, the MIPAS deviations are positive below 100 km (up to  $\sim 0.2$ ), negative between 100 and 115 km (minimum  $\sim -0.15$ ), near zero between 115 and 130 km, and negative between 130 and 170 km (minimum  $\sim -0.2$ ).

Below 90 km, the SMR offsets become progressively more negative compared to the other data sets and the model; we excluded SMR data at these altitudes from the fit. The SMR offsets at these altitudes are due to the inclusion in our analysis of retrievals with low measurement response, which are contaminated by a priori values. Kiviranta et al. (2018) and Pérot and Orsolini (2021) excluded retrievals with measurement responses less than 0.75 and 0.7, respectively; such values occur frequently below 85 km. Figure S1 in Supporting Information S1 shows that the application of such criteria strongly affects the SMR offsets with respect to MSIS 2.1: If retrievals with measurement responses less than 0.7 are excluded, the bias becomes large and positive ( $> 0.5$ ). Figure S1 in Supporting Information S1 also indicates that a simple measurement response criterion cannot fully reconcile the SMR data with the other upper mesosphere data sets; the average offset profile depends strongly on altitude regardless of the cutoff value. Despite these height-dependent offsets, the relative variations (latitude, season, etc.) of the SMR data below 90 km are largely consistent with the other data sets, as shown in subsequent figures.

The SOFIE offsets are somewhat large and positive above 130 km; these data were excluded from the fit. The SCIAMACHY offsets are also increasingly positive above 120 km, which is consistent with the SCIAMACHY-MIPAS comparison presented by Bender et al. (2015, Figure 5).

Figures 6b–6d shows the same analysis but for narrow seasonal-latitudinal bins: Equatorial equinox, mid-high latitude winter, and mid-high latitude summer. The spread of the mean offsets is larger than when all data are combined, but there is no consistent pattern among the data sets that would indicate a major discrepancy in the model. The HALOE offsets vary widely above 120 km among the different seasonal-latitudinal bins but there is relatively little HALOE data at these altitudes, as shown in Figure 2a. Overall, using MSIS 2.1 to approximately filter out average geophysical variations, Figures 6a–6d indicates that the data sets are in systematic agreement with each other to within  $\sim 0.7$  in log space, or approximately a factor of 2. It is evident here and in subsequent



**Figure 6.** (a–d) Average data-minus-model residuals (in natural log space) as a function of altitude, in the seasonal-latitude bins indicated above each panel: (a) all data, (b) equinox (day of year 49–109 plus day 236–296) low latitude, (c) June solstice (day 127–217) southern upper midlatitudes, and (d) June solstice northern upper midlatitudes. All 15 analysis ensembles were included in the averages, along with all of the independent SCIAMACHY daily average data. Only geomagnetically quiet conditions (daily  $A_p \leq 6$ ) are included in the analysis. Results from each data set are coded by color and letter, as indicated in the legend. The altitude bins are 5 km wide from 70 to 140 and 10 km wide from 140 to 200 km. Error bars indicate the  $1\sigma$  estimated uncertainty of the mean. (e–h) The thick gray curves show diurnally averaged MSIS 2.1 nitric oxide (NO) profiles for the approximate average conditions of the data in the upper panels:  $F_{10.7} = 120$  sfu,  $A_p = 4$ , and (a) globally and annually averaged, (b) average of day 79 and 266 profiles at the equator, (c) day 172 at 60°S, and (d) day 172 at 60°N. The superimposed data profiles were calculated by adding the average residual profiles (upper panels) to the model profiles.

analyses that the data sets and model agree best between 90 and 110 km altitude, which is probably attributable to a stronger NO measurement signal in this region of peak NO density.

In order to place the mean residual profiles in the context of the NO density height variation, Figures 6e–6h shows MSIS 2.1 altitude profiles corresponding to the bins used in Figures 6a–6d. Superimposed on the model profiles

are average data profiles computed by adding the average residuals to the model profiles. Note that these are not direct averages of the data but rather averages filtered through MSIS. They represent what we might expect the data to show if the range of geophysical conditions (within each bin) were sampled evenly and identically for each data set. Compared to the amplitude of the NO density height dependence, the mean offsets among the data sets and model are generally small, except for the larger discrepancies noted above. In particular, the broader modeled NO density peak in winter solstice is well supported by the data. Also, the fact that the model accurately follows the vertical gradient of the data (especially SNOE and MIPAS) above 120 km indicates that the MSIS 2.1 thermospheric temperature (which is an independent product of a prior fitting process) and O<sub>2</sub> density (see Section 7) are consistent with the NO density data.

### 5.3. Seasonal-Latitudinal

Figures 7a–7d shows bin-average data-minus-model residuals as a function of latitude, in four selected altitude bins categorized by different physical processes, model formulation, and data behavior. The lowest bin (Figure 7d) is centered on 80 km, where NO density is controlled primarily by dynamical transport processes. The second bin is centered on 100 km, which is near the NO density peak, where photochemistry dominates. The third bin is centered on 120 km, near where the model formulation transitions from a cubic spline basis to a hydrostatic profile coupled to temperature (see Section 2.1). In the fourth bin, 140–150 km, NO is fully coupled to temperature in the model (and to O<sub>2</sub> in the real thermosphere) and is a key contributor to the thermospheric heat budget (e.g., Mlynarczyk et al., 2021). Results are shown for June solstice conditions.

In the upper three altitude bins, the mean residuals do not show any latitudinal patterns that are consistent among the data sets, indicating that the model has captured the average latitude dependence in the data to within the systematic differences of the data sets. At 80 km, however, the residuals show a consistent “w” shaped pattern, indicating that the model has not fully captured the latitude dependence in the data (nonetheless, the model agrees with the data typically to within  $\pm 0.3$  in natural log space ( $\sim 35\%$ )). Note that even though the SMR data have a large negative offset at this altitude, the latitudinal pattern is similar to that of the other data sets.

To better understand the significance of the mean residuals, we adapt the multilinear regression approach of partial residuals (e.g., Chatterjee & Hadi, 2009) to isolate the average dependence of the data on individual geophysical variables. The technique consists of turning off the model terms involving the target variable prior to computing residuals, which effectively filters out the estimated mean dependence on all other variables, so that the resulting partial residuals should approximately only exhibit the target variation. This approach (cf., Emmert & Picone, 2010) mitigates sampling differences among data set, and thereby permits the use of larger bins to reduce the uncertainty of the mean. It also provides a way of graphically assessing the magnitude of a variation in the data relative to the variance of the mean total residuals. Note that the mean altitude dependence presented in Figures 6e and 6f is similar to a partial residual approach but in MSIS it is not possible to turn off the altitude dependence, so in those figures the mean residuals were instead applied to the model profiles a posteriori.

To compare the mean partial residuals with MSIS, we further calculate model cuts with the target variation turned on. Depending on the data bins selected for other model variables, we either switch those terms off or evaluate the model at the average value of each variable within the data bin, as appropriate. In this way, the model cut should approximately follow the average variation seen in the partial residuals, if the model is accurately representing that variation.

Figures 7e–7h applies and illustrates the partial residual technique for the latitude dependence of the data and model. Latitude and season are strongly coupled for NO density (and for most other atmospheric state variables), such that the stand-alone variations (i.e., the annual-average latitude dependence and the global-average day of year dependence) are relatively weak compared to the coupled variation. Accordingly, Figure 7 examines the latitude dependence at a specific time of year (June solstice, with data from a 90-day bin centered on the solstice). To calculate partial residuals, we evaluated the model with the latitude-only and coupled season-latitude terms turned off. For the model cuts, we evaluated the model with those terms turned on, along with the  $\bar{F}_{10.7}$  dependence, at the centers of the season and altitude bins and for the average  $\bar{F}_{10.7}$  of all the data in each season-altitude bin. All other model terms (geomagnetic activity, local time, and longitude) were turned off when computing model cuts. The data used in the analysis were restricted to geomagnetically quiet conditions (daily  $A_p \leq 6$ ),

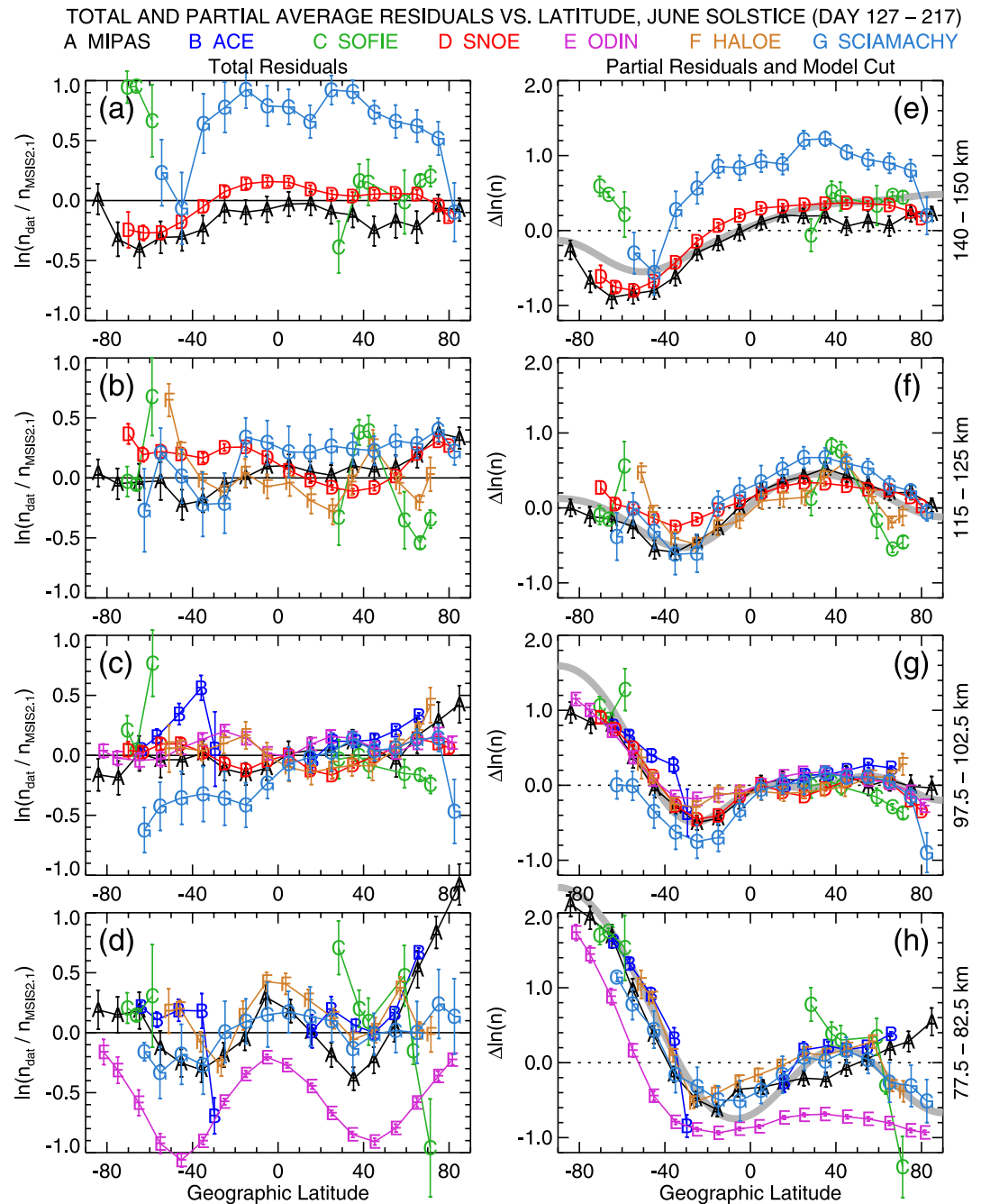


**Figure 7.** (a–d) Average data-minus-model total residuals as a function of geographic latitude, for June solstice (day of year 127–217), geomagnetically quiet ( $A_p \leq 6$ ) conditions, and in the four altitude bins indicated to the right of each row of panels. All 15 analysis ensembles were included in the averages, along with all of the independent SCIAMACHY daily average data. Results from each data set are coded by color and letter, as indicated in the legend. The latitude bins are  $10^\circ$  wide, from  $90^\circ\text{S}$  to  $90^\circ\text{N}$ . Error bars indicate the  $1\sigma$  estimated uncertainty of the mean. (e–h) Same analysis as the left panels, except that the MSIS 2.1 latitudinal and seasonal-latitudinal terms were turned off prior to calculating the residuals, effectively filtering out from the data all modeled variations other than seasonal-latitudinal. The thick gray curve shows the quiet-time, diurnally averaged MSIS 2.1 latitudinal variation corresponding to the average  $F_{10.7}$  conditions of the data in each altitude bin. The dotted horizontal line marks the latitudinally averaged (weighted by cosine latitude) model value to which the model cut and partial residuals are referenced.

which produces approximately the same average  $A_p$  values as the quiet-time reference value used by MSIS ( $A_p = 4$ ), so turning off the geomagnetic activity dependence has approximately the same effect as keeping it on and evaluating the model at the average  $A_p$  of the data.

The results in Figures 7e–7h confirm that the model is accurately reproducing the latitude dependence seen in the average partial residuals to within the spectral resolution of the model and the variance among the mean residuals of the different data sets. At 80 km, Figure 7h suggests that the w-shaped pattern in the total residuals (Figure 7d) is caused by insufficient spectral resolution (i.e., the low-order truncation of the spherical harmonic basis) in the model. The data show a pattern of approximately linearly decreasing log density from 70°S to 20°S, followed by a linear increase toward northern summer latitudes. Legendre functions are not well suited to represent such a piecewise-linear pattern. We experimented with increasing the spectral resolution to degree 6 (we truncated at degree 4 in the fit, as discussed in Section 4.3) but that did not improve the fit. Further consideration of the model formulation is therefore necessary to address this discrepancy.

Figures 7e–7h also directly illustrate the shift in the seasonal-latitudinal phase of the data with altitude. Consistent with Figure 4, below ~110 km the NO density maximizes in the winter hemisphere (due to less photolysis), whereas above ~120 km it maximizes in the summer hemisphere (due to coupling with the warmer summer temperature). We obtained similar results for December solstice (not shown).

Figure 8 presents the same analysis as Figure 7 but focusing on the seasonal dependence at northern high latitudes. At 120 km and 145 km, the mean total residuals (Figures 8a and 8b) are flat with respect to day of year, to within the offsets among the data sets. At 100 km and 80 km (Figures 8c and 8d), most of the data sets are consistently smaller than the model near day 100 (just after the March equinox); the magnitude of this dip ranges from 0 to 0.7 (i.e., up to a factor of ~2). A similar but smaller and less consistent dip is evident near the September equinox. The partial residuals shown in Figures 8g and 8h indicate that the shape of the seasonal variation at these latitudes and altitudes is not optimally represented by the annual harmonic terms used in the model. Instead of a pure sinusoid, the NO density decreases rapidly from winter to spring equinox as the high latitudes emerge from polar night and NO is depleted by photodissociation, followed by a more gradual increase from summer back to the winter. The addition of semiannual harmonic terms to the model fit might provide a better representation of the data and should be considered in future model development.

#### 5.4. Solar Activity

At low and midlatitudes, NO density is known to increase with increasing solar flux: The greater intensity of soft X-rays at solar maximum produces more energetic secondary electrons and hence increased NO production (Barth et al., 1988; Fuller-Rowell, 1993; Marsh et al., 2004). Figure 9 shows average total and partial residuals near the equator as a function of solar activity on timescales longer than 81 days, as represented by  $\bar{F}_{10.7}$ . The total residuals are largely flat at all altitudes, indicating that the model is accurately representing the mean solar cycle dependence of the data. At 120 km, the MIPAS, SCIAMACHY, and HALOE data decrease slightly relative to the model from  $\bar{F}_{10.7} = 80$  to 140 sfu (the definitions and notation of the  $F_{10.7}$  terms are given in Equation 3), but this behavior is not evident in the SNOE data.

The partial residuals shown in Figures 9c–9g demonstrate that the model is accurately representing the nonlinear dependence of the data on  $\bar{F}_{10.7}$  at altitudes of 100 km and above, over the entire range of solar activity covered by the data. The density increases by a factor of ~4 from solar minimum to solar maximum; most of the increase occurs at  $\bar{F}_{10.7}$  levels below 100 sfu. At 80 km, the dependence is very weak in the model and not apparent in the data.

Figures S2 and S3 in Supporting Information S1 show the same analysis at high southern and northern latitudes, respectively. The solar cycle dependence is weaker overall than at low latitudes. At 100 km and 80 km, the model NO density decreases slightly for  $\bar{F}_{10.7} > 120$  sfu. This decrease is weakly supported by the HALOE and SNOE data. Marsh et al. (2004) and Hendrickx et al. (2018) noted anticorrelations of NO density data (SNOE and SOFIE, respectively) with solar flux at high latitudes that are possibly consistent with the MSIS 2.1 results. Marsh et al. (2004) speculated that the SNOE NO decrease may be due to the suppression of discrete auroral arcs at solar maximum, or to indirect effects of lower thermospheric temperature and composition on the balance of NO production and loss.



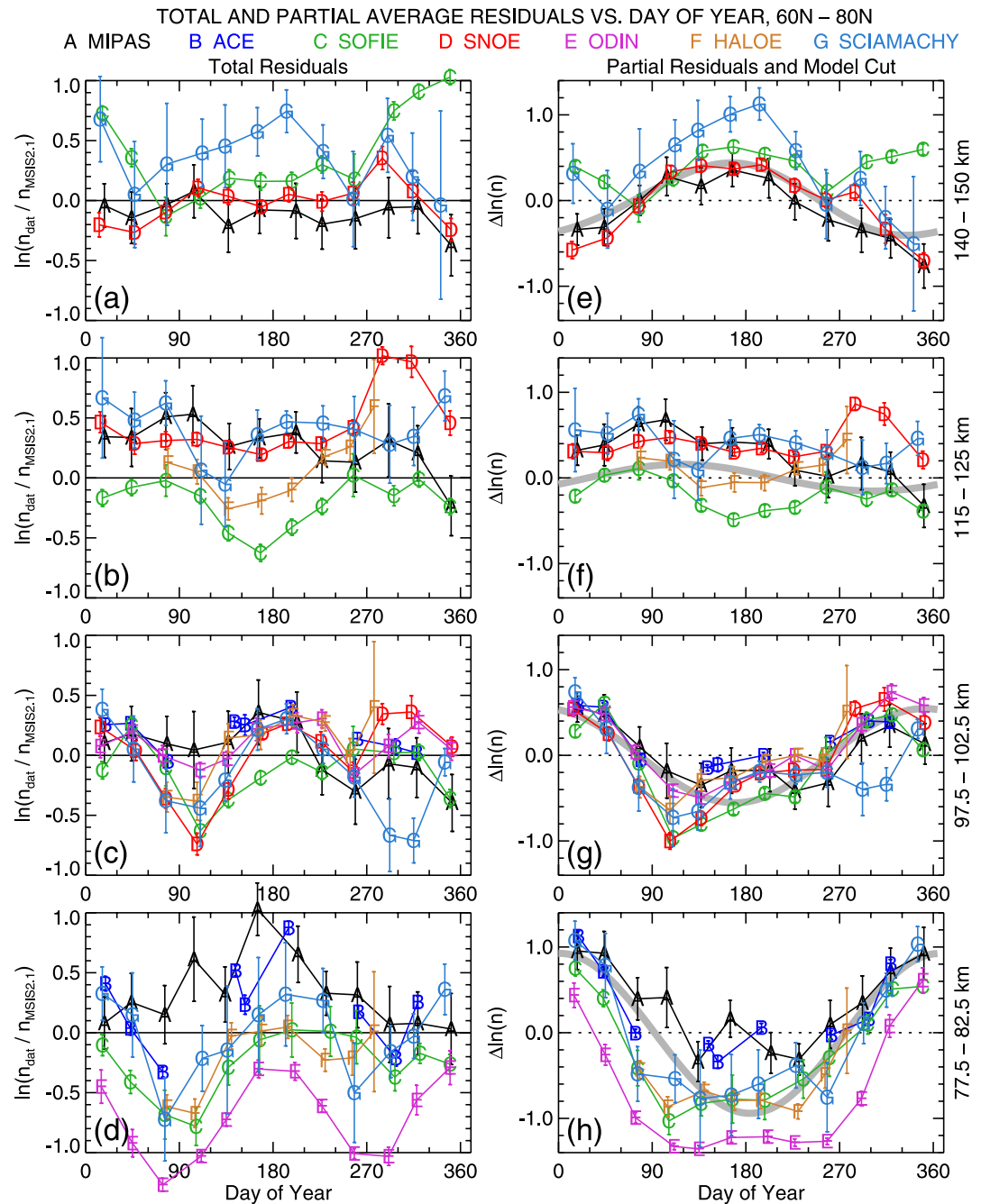


**Figure 8.** Same analysis as Figure 7, but as a function of the day of year, at northern high latitudes (60°–80°N). The day of year bins are 30.5 days wide (approximately monthly bins). In panels (e–h) on the right, the thick gray curve shows the day-of-year variations of the model referenced to the annual average.

The solar cycle dependence of the data is strongest at low and midlatitudes in both the data and the model, as illustrated in Figure S4 in Supporting Information S1. The strength of the  $\bar{F}_{10.7}$  dependence is fairly constant between 40°S and 40°N, decreasing at higher latitudes approximately linearly toward the poles. This behavior of the data is well captured in the model via the  $P_{2,0}$  and  $P_{4,0}$  latitudinal modulation of the  $\bar{F}_{10.7}$  terms.

Hendrickx et al. (2015) detected a 27-day variation in SOFIE NO density associated with the solar rotational period. They attributed this variation to NO production by energetic particle precipitation, using a superposed epoch analysis with respect to the auroral electrojet (AE) index, in which both the NO data and AE were



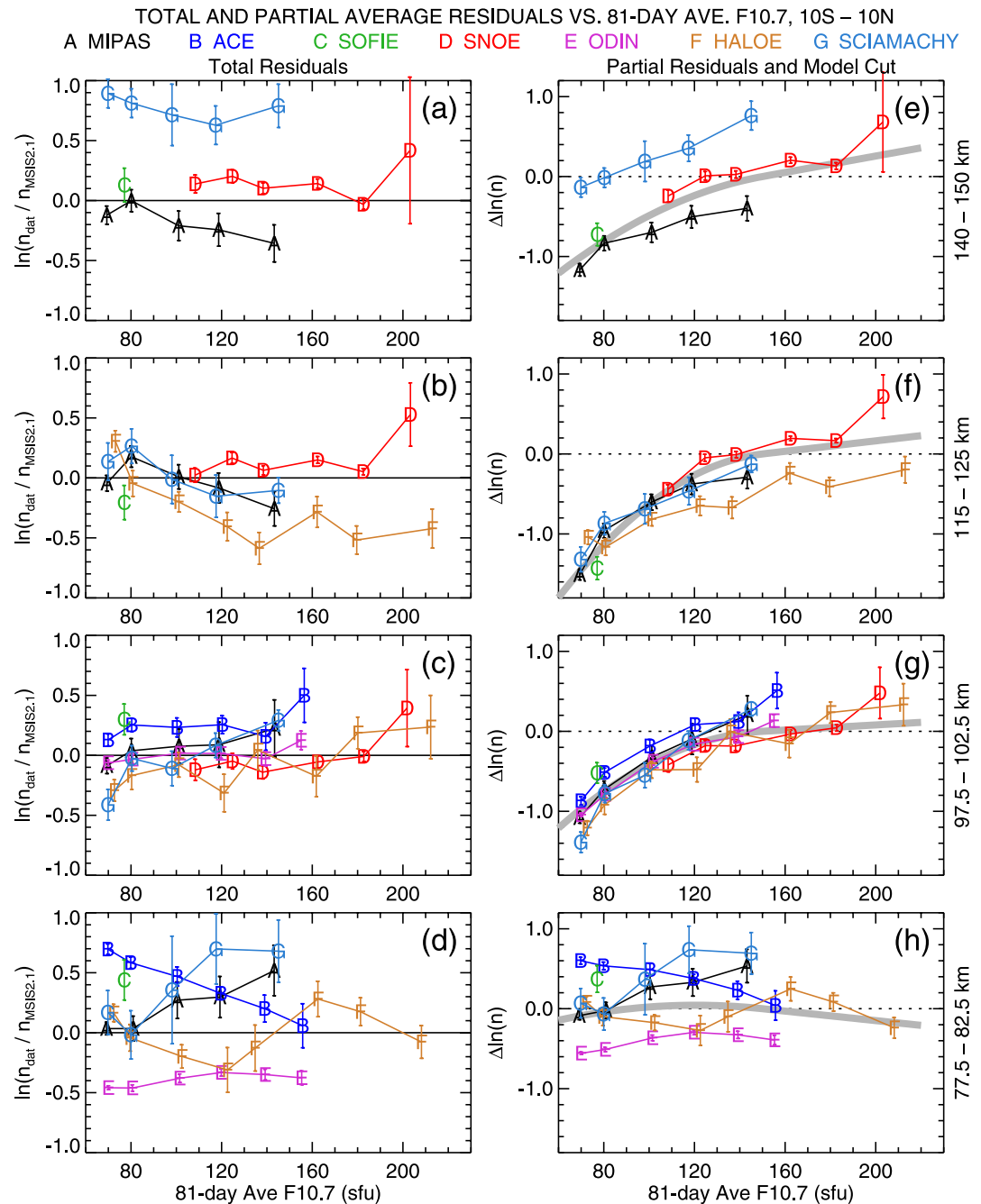


**Figure 9.** Same analysis as Figure 7, but as a function of  $\bar{F}_{10.7}$  (the 81-day average of the daily  $F_{10.7}$ ), near the equator ( $10^{\circ}\text{S}$ – $10^{\circ}\text{N}$ ), and including data from all times of the year. The  $\bar{F}_{10.7}$  bins are 65–75, 75–90, 90–110, 110–130, 130–150, 150–170, 170–200, and 200–230. In panels (e–h) on the right, the partial residuals were calculated relative to MSIS 2.1 with the  $\bar{F}_{10.7}$  terms and the coupled  $\bar{F}_{10.7}$ –latitude terms turned off. The thick gray curve shows the  $\bar{F}_{10.7}$  variation of the model referenced to the model value at  $\bar{F}_{10.7} = 150$  sfu.

preprocessed with a 27-day high-pass filter. In MSIS 2.1, variations on daily to 27 days timescales are represented by the  $\Delta F_{10.7}$  and  $A_p$  geomagnetic activity terms. The 27 days solar rotational cycle is most evident in  $F_{10.7}$ , and Figure 10 examines the total and partial residual dependence of the data on  $\Delta F_{10.7}$  at low and midlatitudes. Near 100 km, the model NO density increases by  $\sim 42\%$  ( $\sim 0.35$  change in log density) in response to a 50 sfu enhancement in the daily  $F_{10.7}$ .

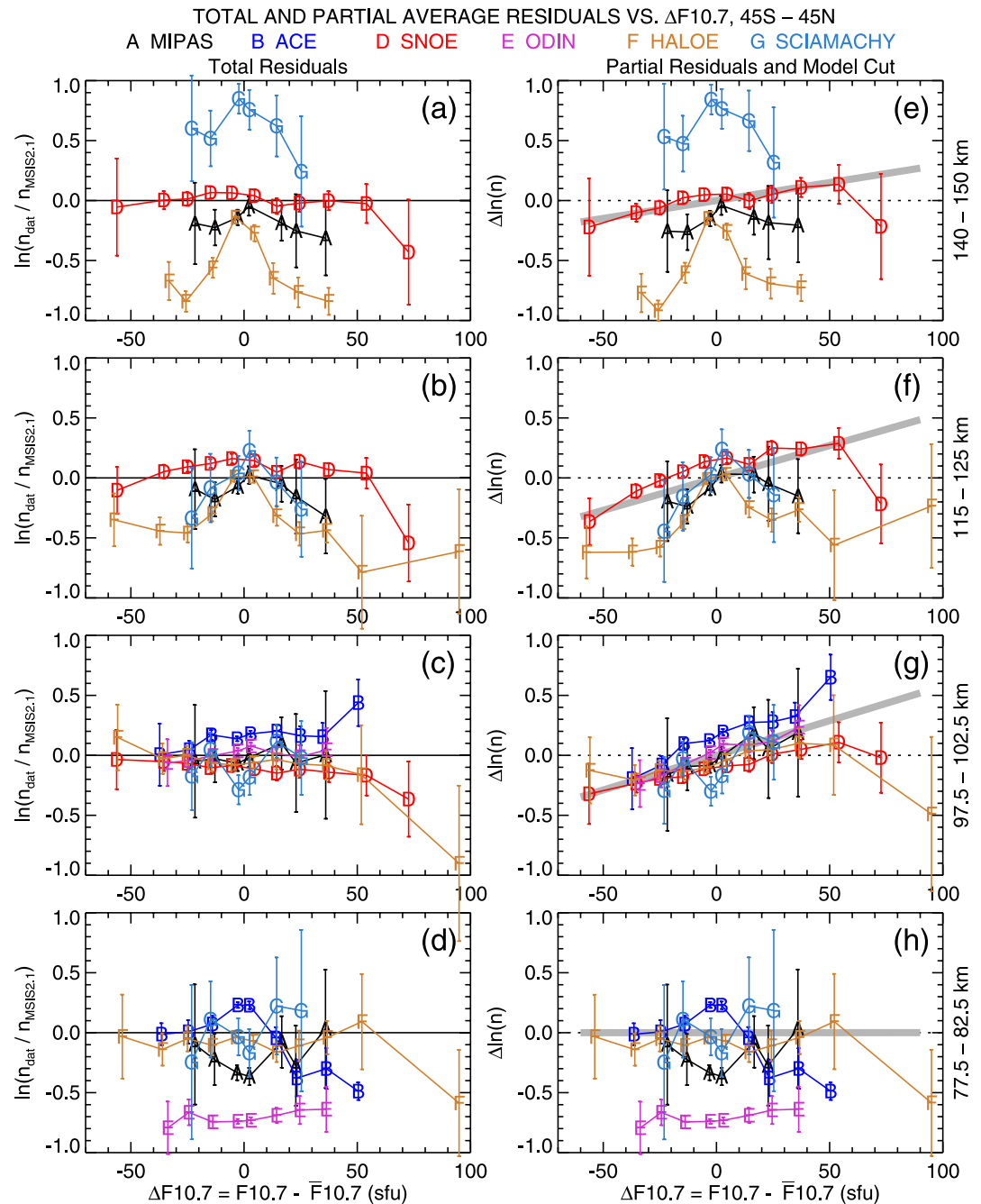


**Figure 10.** Same analysis as Figure 7 but as a function of  $\Delta F_{10.7} = F_{10.7} - \bar{F}_{10.7}$ , where  $\bar{F}_{10.7}$  is the 81-day average of the daily  $F_{10.7}$ , at low and midlatitudes (45°S–45°N) and including data from all times of the year. The  $\Delta F_{10.7}$  bins are  $\pm 0$ –10,  $\pm 10$ –20,  $\pm 20$ –30,  $\pm 30$ –50, and  $\pm 50$ –100 sfu. In panels (e–h) on the right, the partial residuals were calculated relative to MSIS 2.1 with the  $\Delta F_{10.7}$  term and the coupled  $\Delta F_{10.7}$ –latitude term turned off. The thick gray curve shows the  $\Delta F_{10.7}$  variation of the model referenced to the model value at  $\bar{F}_{10.7} = 150$  sfu and  $\Delta F_{10.7} = 0$ .

To further explore the short-term variability in the data attributable to solar flux at solar rotation timescales, Figure 11 shows average partial residuals near 100 km as a function of time (in 7.5 days bins), for the years 1999 and 2012. The residuals were computed relative to MSIS 2.1 with the  $\Delta F_{10.7}$  terms turned off. There are clear variations in the partial residuals that are consistent among the data sets. These variations visually correspond to and are moderately correlated with  $\Delta F_{10.7}$  variations, which are dominated by the 27-day rotational cycle during

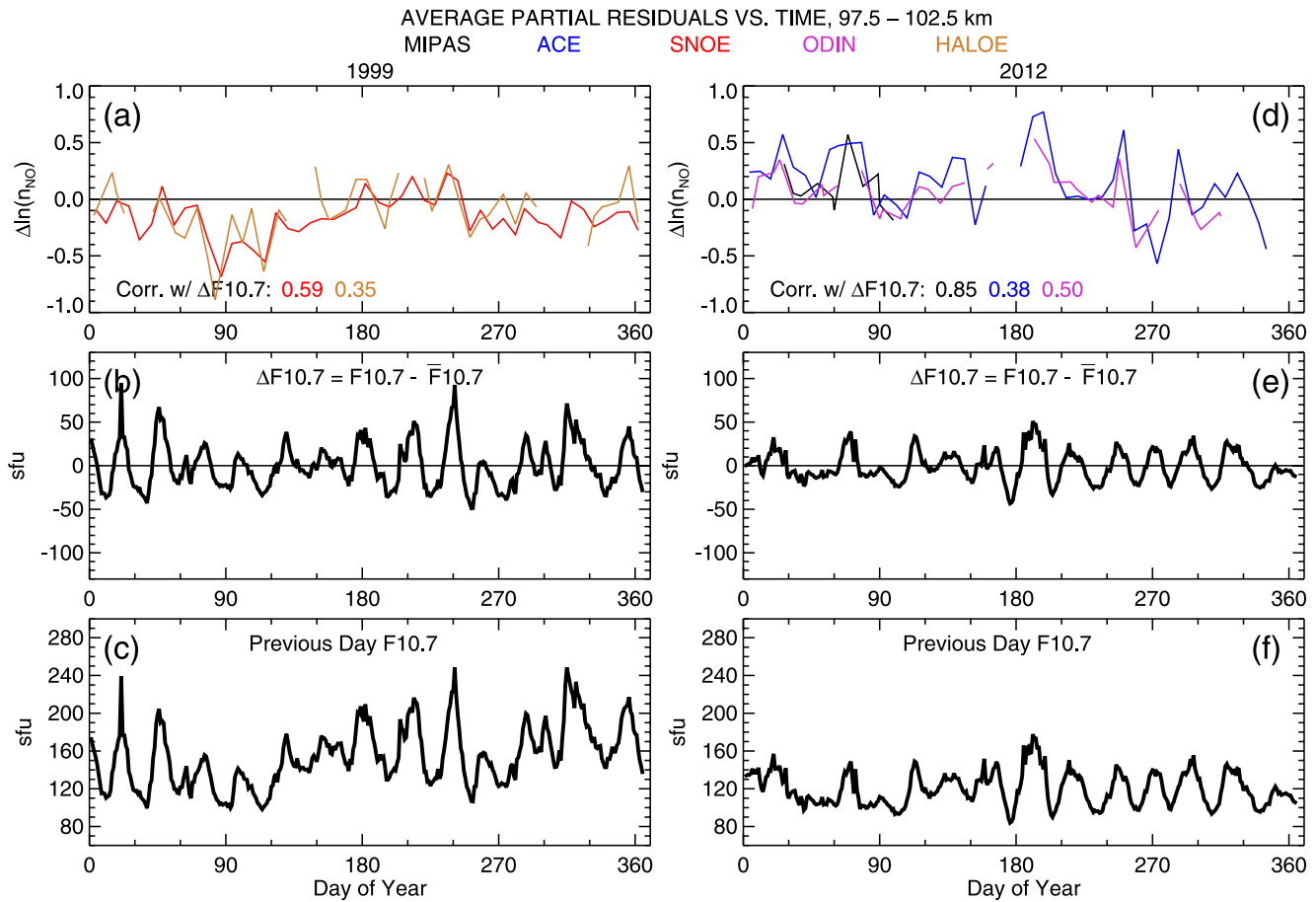


**Figure 11.** (a) Average partial data-minus-model residuals, as a function of time in 1999, relative to MSIS 2.1 with the  $\Delta F_{10.7}$  terms turned off, thereby highlighting the short-term variations in the data that are partly attributable to  $F_{10.7}$  variations. The residuals were averaged in 7.5 days bins. Results from each data set are coded by color, as indicated in the legend. The analysis used data from all latitudes and geomagnetic activity levels, in the altitude range 97.5–102.5 km. (b)  $\Delta F_{10.7}$  as a function of time. (c) Previous day daily  $F_{10.7}$  as a function of time. Panels (d–f) same as panel (a–c), but showing results for the year 2012. The Pearson correlation coefficients of the average partial residuals and  $\Delta F_{10.7}$  are annotated in panels (a and d).

the selected years. This is qualitatively consistent with the findings of Hendrickx et al. (2015). Figure S5 in Supporting Information S1 presents similar results for the years 1998 and 2011.

### 5.5. Geomagnetic Activity

At high latitudes, NO is produced via energetic particle precipitation (e.g., Maeda et al., 1989). NO density therefore increases with increasing geomagnetic activity. Figure 12 shows average total and partial residuals at high southern latitudes as a function of the daily average  $Kp$  index. The average total residuals (Figures 12a–12d) do not exhibit any consistent departures from flatness (with one possible exception addressed below), indicating that the model is capturing the geomagnetic activity dependence in the data to within the variance among the data sets. These residuals were computed with respect to MSIS 2.1 in the daily geomagnetic activity mode (which depends solely on the daily  $Ap$  index). We also validated the model in storm-time mode (which depends on the time history of the 3 hr  $ap$  index) as a function of the local 3 hr  $Kp$  index and found similar good agreement between the model and data sets (not shown).

At 100 km and above, Figures 12e–12g indicates that the  $Kp$  dependence in the data saturates above  $Kp = 3$ –4. The model captures this saturation reasonably well. At 100 km, the model NO density increases by a factor of  $\sim 1.8$  from the quietest levels to the saturation level. At 120 km, the increase is slightly larger, a factor of  $\sim 2$ . At 145 km, the geomagnetic activity dependence of temperature, which does not saturate in the model, reduces the

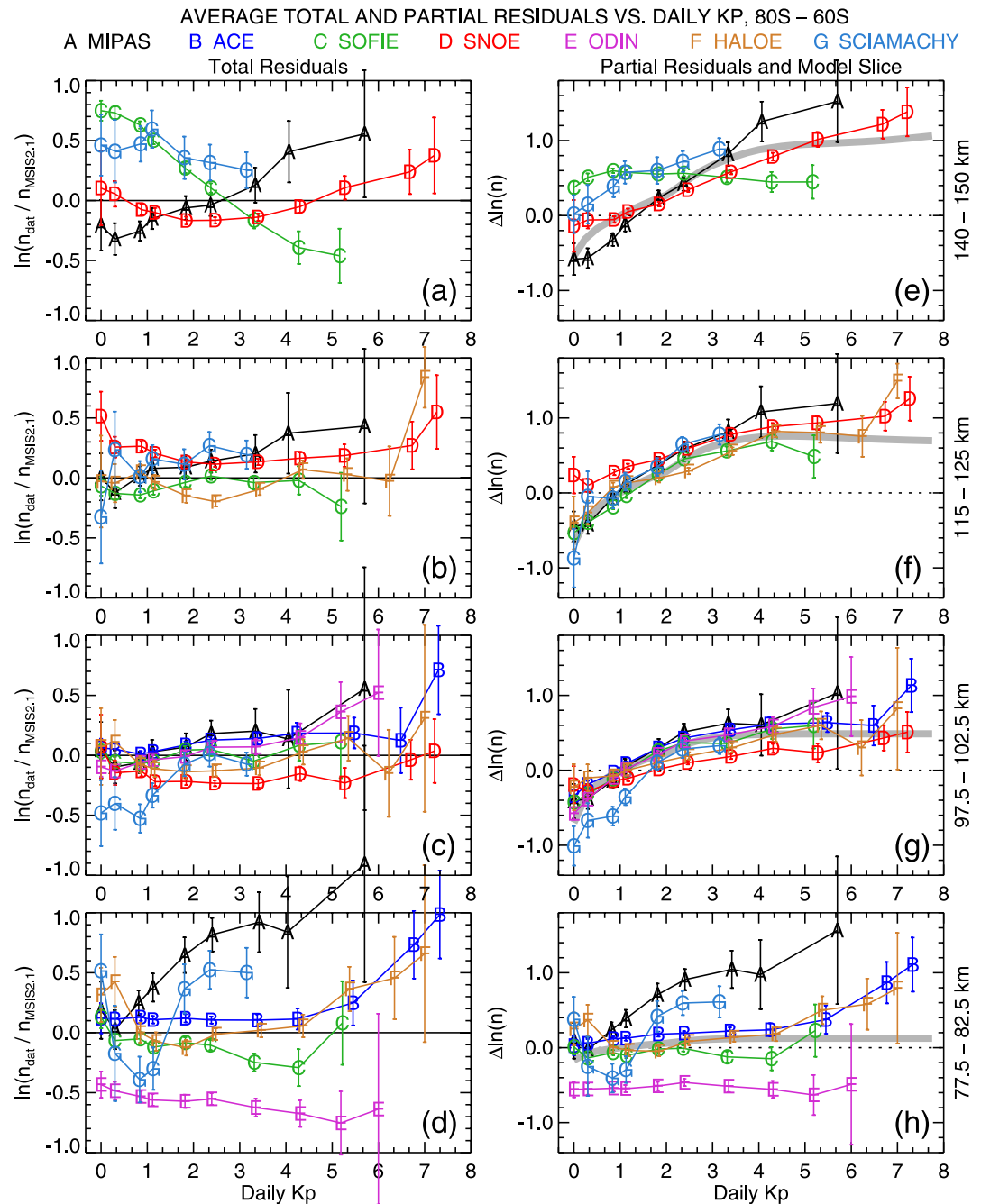


**Figure 12.** Same analysis as Figure 7 but as a function of the daily average  $Kp$  index of geomagnetic activity, at southern high latitudes ( $80^{\circ}$ – $60^{\circ}$ S), and including data from all times of year and solar activity conditions. The  $Kp$  bins are 0–0.3, 0.3–0.7, 0.7–1, 1–1.5, 1.5–2, 2–3, 3–4, 4–5, 5–6, 6–8, and 7–9. In panels (e–h) on the right, the partial residuals were calculated relative to MSIS 2.1 with the global and latitude-modulated geomagnetic activity terms turned off. The thick gray curve shows the  $Kp$  variation of the model referenced to the model value at  $Kp = 1$  ( $A_p = 4$ ).

saturation effect in the NO density, so that the modeled NO density continues to increase slightly at  $Kp$  values greater than 4.

At 80 km, the modeled geomagnetic activity dependence is weak. This is consistent with the data up to at least daily  $Kp = 4$ . At higher levels, the ACE and HALOE data suggest that there is an enhancement of NO, increasing to a factor of  $\sim 2$  at  $Kp = 7$ . This effect is also evident, but not as clear, at northern high latitudes, as shown in Figure S6 in Supporting Information S1. This behavior of the data may be a reflection of downward transport

of NO during intense geomagnetic storms (e.g., Harvey et al., 2021; Smith et al., 2011; and references therein). Alterations in the MSIS formula would be necessary to capture this effect, including a more tailored treatment of the geomagnetic activity time history and possibly coupling with the seasonal dependence.

Figure S7 in Supporting Information S1 illustrates and validates the latitudinal modulation of the  $Kp$  dependence. The effect increases from near zero at the equator to its maximum at high latitudes.

### 5.6. Local Time

As discussed in Section 2, none of the data sets considered here provide continuous local time coverage. Thus, it is very difficult to distinguish between local time variations and offsets among the data sets. Nonetheless, we found that the model appears to adequately represent the local time dependence to within the variance among the data sets. This is illustrated in Figure 13, which shows average partial residuals as a function of local time within

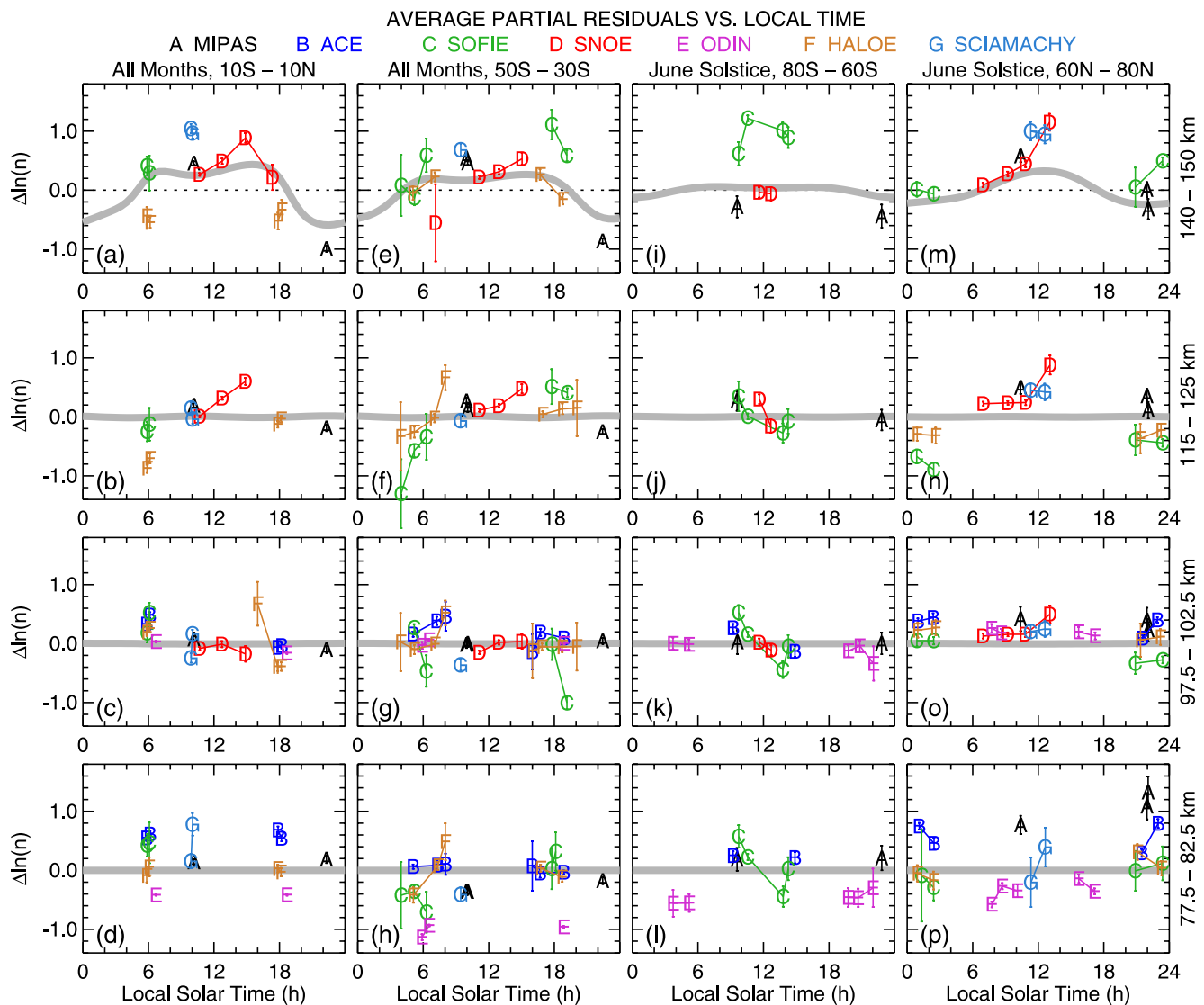


**Figure 13.** Average partial residuals, relative to MSIS 2.1 with the local time and solar zenith angle terms turned off, as a function of local time. Results are shown for the following seasonal-latitude bins: (a–d) all months near the equator, (e–h) all months at southern midlatitudes, (i–l) June solstice (day 127–217) at southern high latitudes, and (m–p) June solstice at northern high latitudes. Results are shown for geomagnetically quiet ( $A_p \leq 6$ ) conditions in the four altitude bins indicated to the right of each row of panels. Results from each data set are coded by color and letter, as indicated in the legend. The local time bins are 2 hr wide. Error bars indicate the  $1\sigma$  estimated uncertainty of the mean. The thick gray curves show the MSIS 2.1 local time variation corresponding to the approximate average conditions of the data in each panel. The dotted horizontal line marks the diurnally averaged model value to which the model cut and partial residuals are referenced.

selected seasonal-latitudinal bins. At 120 km and below, the model local time dependence (implemented via SZA terms as described in Section 4.2) is very weak, which is consistent with statistical spread of the available data sets.

Siskind et al. (2019) compared low-latitude SOFIE NO profiles measured near dawn with the NOEM empirical model (which is based on SNOE data near 11 LT), finding that the SOFIE and NOEM profiles have similar peak densities but the SOFIE profile peaks 6–8 km lower than NOEM. They found that this behavior is consistent with TIME-GCM simulations constrained by middle atmospheric wind and temperature data, and they attributed it to advection of NO by migrating solar tides. The data shown in Figures 13b and 13c are qualitatively consistent with the SOFIE and NOEM profiles shown in Figure 2 of Siskind et al. (2019): At 120 km (above the NO peak), SOFIE densities are 20%–30% smaller than SNOE/NOEM but at 100 km (below the NOEM peak but at the SOFIE peak in Siskind et al. (2019)) SOFIE densities are ~80% larger than SNOE/NOEM. The HALOE results in Figures 13b and 13c show similar behavior relative to SNOE at 120 and 100 km. Siskind et al. (2019) argue that this variation is due to the semidiurnal tide, which is currently not used in the MSIS 2.1 NO formulation.

At 145 km, the local time dependence in the model is driven by the diurnal tide in the MSIS temperature, with larger values during warmer daytime conditions. At the equator (Figure 13a), the daytime MSIS NO density is ~65% larger than at night. MIPAS, which is the only data set that covers both day and night conditions at this altitude, indicates a slightly larger day-night difference. Similar results are found at midlatitudes (Figure 13e). At summer high latitudes (Figure 13m), the diurnal temperature variation over the sunlit polar region results in a ~35% change in MSIS NO density; the MIPAS measurements at 10 and 22 LT are consistent with this amplitude.

Additional plots of both total and partial averages versus local time are provided in Figures S8 in Supporting Information S1 (equator) and Figure S9 in Supporting Information S1 (northern winter high latitudes).

Given that MSIS represents NO all the way to the poles and that most of the measurements are made under sunlit or terminator conditions, it is worthwhile to examine more closely how the model represents polar winter conditions, where the data are sparsest. Although local time is largely irrelevant geophysically in this region, the data are strongly aligned with local time, so we consider polar winter coverage in this section. Figure 14 shows the latitude and local time variation of the model at 100 km altitude over the northern and southern winter poles, along with the corresponding data coverage within 15 days of the solstices. The model patterns are concentric as a result of the very weak local time dependence. The polar nighttime region is bounded by the solar terminator (SZA ~ 100°) marked by the dashed white line. MIPAS and SMR are the only measurements in this region; the other data sets are daytime (SNOE) or SZA = 90° (ACE, SOFIE). The model thus represents the polar night region directly via the MIPAS and SMR data and by latitudinal extrapolation (using the Legendre function basis) via the other data sets. Figure 7 (Southern Hemisphere) indicates that the model accurately represents the data and its latitudinal trends under these conditions. Figures 13k, 13l and Figure S9 in Supporting Information S1 support the lack of a significant local time variation within the polar night region.

## 6. Comparison With NOEM

NOEM (Marsh et al., 2004) is an empirical model of SNOE 1998–2000 data as a function of altitude (100–150 km, at 3.33 km intervals), geomagnetic latitude (80°S–80°N, at 5° intervals), solar declination, daily  $K_p$ , and daily  $F_{10.7}$ . There are several key differences between the construction of NOEM and MSIS 2.1 NO. First, the NOEM model is a fit of number density, whereas the internal dependent variable in the MSIS formulation is log number density. Second, in contrast to the parametric altitude and latitude formulation of MSIS 2.1 NO (explicitly coupled to temperature above 110 km), the latitude and altitude dependence of NOEM is represented by empirical orthogonal functions (EOFs). Motivated by the patterns of the first three EOFs, NOEM modulates these EOFs, respectively, as a linear function of daily  $K_p$ , a third-order polynomial in solar declination, and a linear function of  $\log(F_{10.7})$ . Third, NOEM uses geomagnetic latitude, whereas MSIS uses geographic latitude.

Figure 15 compares MSIS 2.1 and NOEM log density as a function of altitude and latitude (geographic for MSIS, geomagnetic for NOEM). Results are shown for four selected seasonal, solar activity, and geomagnetic activity conditions: June solstice (top 2 rows) and September equinox (bottom 2 rows); solar minimum (top row) and solar maximum (bottom 3 rows); and geomagnetically quiet (top 3 rows) and disturbed (bottom row). At solar minimum, the NOEM densities are typically 2–7 times larger than MSIS, with the largest differences occurring



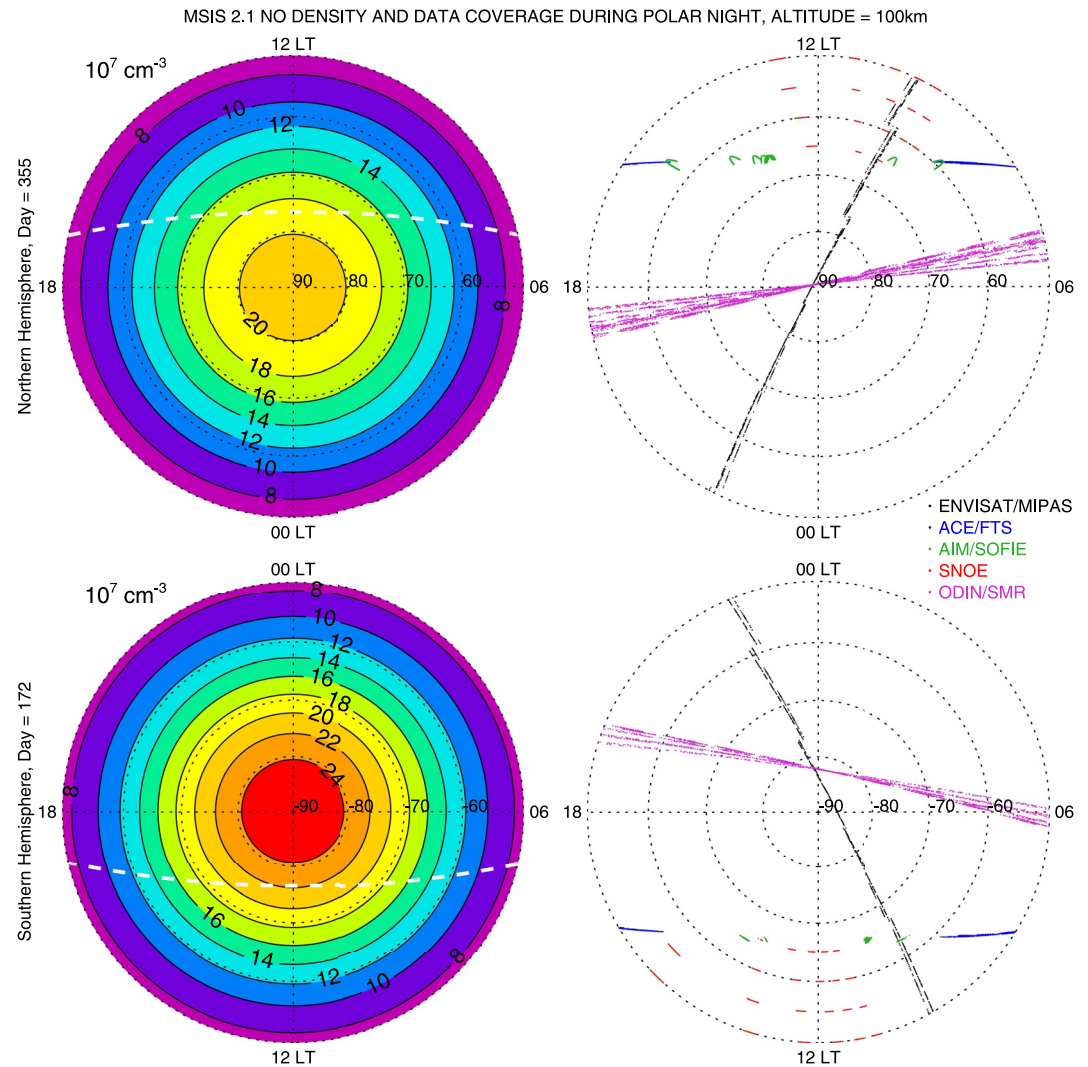


**Figure 14.** (Left) Latitude and local time variation of MSIS 2.1 nitric oxide (NO) density at 100 km altitude, over (top) the North Pole at December solstice and (bottom) the South Pole at June solstice. The contour interval is  $2 \times 10^7 \text{ cm}^{-3}$ . The dashed white line marks the solar terminator at 100 km (solar zenith angle =  $100^\circ$ ). (Right) Corresponding data coverage under the winter solstice conditions. The data locations shown are from all 15 fitting ensembles, including altitudes from 95 to 105 km and times within 15 days of the winter solstice.

near 120 km at winter high latitudes (in contrast, in Figure 9c the average deviations of the data sets from MSIS are typically less than  $\sim 35\%$  across all solar activity levels). This difference is likely due to the relative lack of solar minimum data available to NOEM. Also, Figure 4c of Marsh et al. (2004) indicates that below  $F_{10.7} = 110$  sfu, NOEM predicts larger density than the SNOE data that is available. In contrast, MSIS 2.1 is well supported by solar minimum data, as illustrated in Figure 9.

Under solar maximum conditions, MSIS 2.1 and NOEM are in much better agreement, generally within 20% at low and midlatitudes. During September equinox at northern high latitudes, NOEM is up to 80% larger ( $\sim 0.6$  in natural log space) than MSIS. This Northern Hemisphere difference also occurs during March equinox and December solstice but does not occur in the Southern Hemisphere in any season (not shown). In Figures 2a and 2b of Marsh et al. (2004), both the mean and EOF 1 (ascribed to geomagnetic activity) are larger in the Northern Hemisphere. Our Figures S6f, S6g, S7f and S7g in Supporting Information S1 indicate a similar hemispheric asymmetry but only under elevated geomagnetic activity conditions. This feature warrants further study; capturing it in MSIS would require the addition of asymmetric latitudinal terms modulating the geomagnetic activity dependence (currently, only the symmetric  $P_{2,0}$  and  $P_{4,0}$  Legendre functions are used).

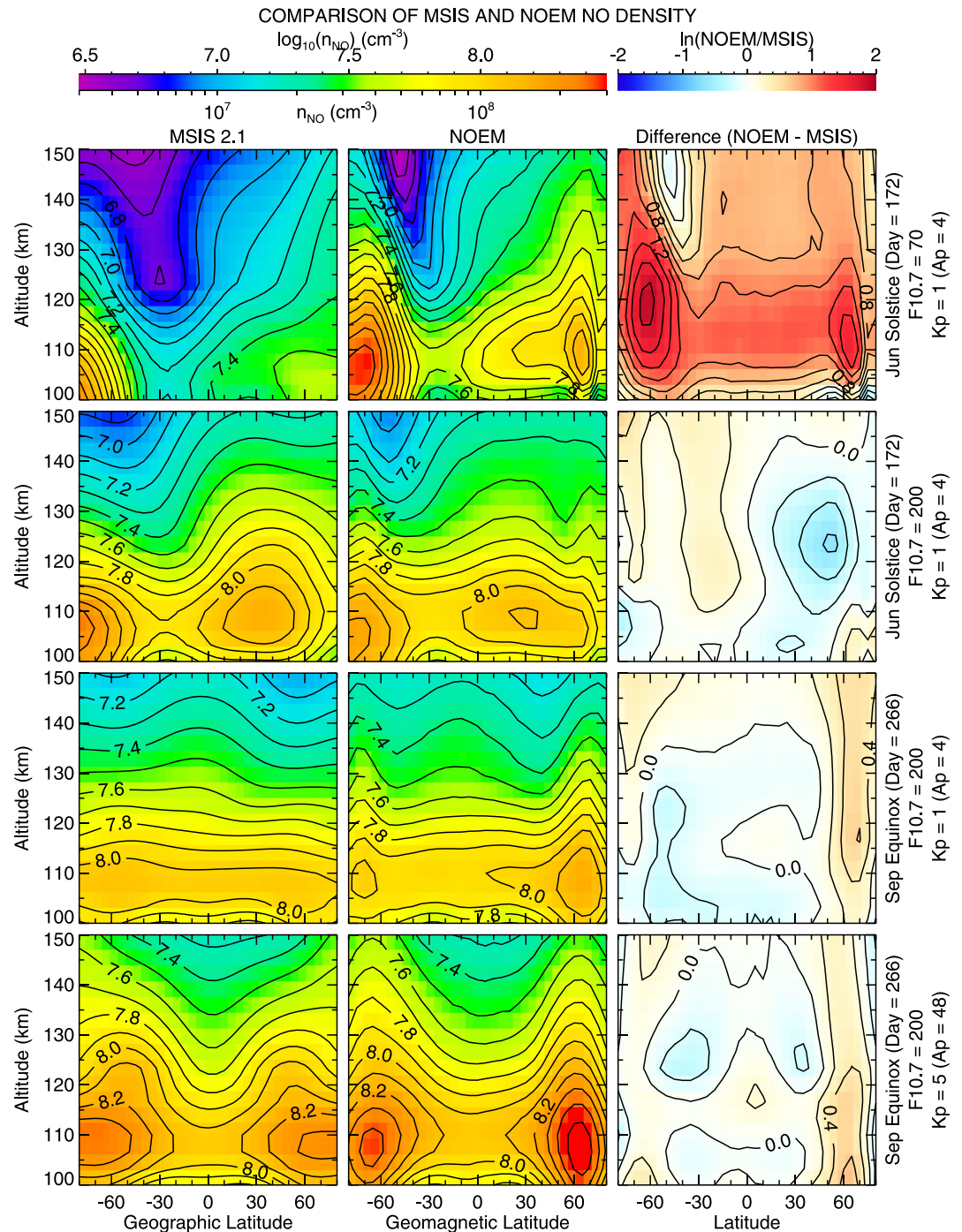


**Figure 15.** (Left) MSIS 2.1  $\log_{10}$  nitric oxide density at 1100 local time, as a function of altitude (100–150 km) and geographic latitude (80°S–80°N), for the geophysical conditions indicated to the right of each row. The contour interval is 0.1 (~26% increase with each successively higher contour). (Center) Corresponding Nitric Oxide Empirical Model (NOEM; Marsh et al., 2004) density, as a function of altitude and geomagnetic latitude. (Right) Natural log of the NOEM/MSIS ratio. The contour interval is 0.2 (~22%).

Another key difference between NOEM and MSIS 2.1 is that the NOEM density peaks near 65° geomagnetic latitude, whereas MSIS has broader peaks in geographic latitude. The difference is a result of preferential NO production in the auroral zone, which is organized in geomagnetic coordinates. Figure S10 in Supporting Information S1 shows average quiet-time total residuals with respect to MSIS 2.1 as a function of geomagnetic latitude

in  $5^\circ$  bins, which is the resolution of NOEM. Localized enhancements are evident near  $70^\circ$  at altitudes from 100 to 120 km, confirming that additional terms are needed to capture this feature in MSIS. This could be accomplished either by activating the longitude terms in MSIS for NO or by introducing new terms in geomagnetic latitude. Below 100 km, the average residuals are essentially flat as a function of geomagnetic latitude, likely because the direct production by auroral activity is weaker at these altitudes. Above 120 km, the residual auroral enhancements also disappear, probably in part because the NO density becomes strongly coupled to temperature, which in MSIS includes longitudinal and UT variations that address the geomagnetic latitude dependence.

Figure S11 in Supporting Information S1 compares NOEM and MSIS 2.1 as a function of latitude and  $F_{10.7}$  (for MSIS, the same  $F_{10.7}$  values were used for both the daily and 81-day average) for geomagnetically quiet June solstice conditions. As discussed above, NOEM densities are larger than MSIS 2.1 at solar minimum. This difference decreases with increasing  $F_{10.7}$ , generally becoming near-zero between 120 and 160 sfu, depending on altitude and latitude. Between 110 and 130 km, NOEM becomes smaller than MSIS 2.1 for  $F_{10.7}$  values above  $\sim 160$  to 200 sfu.

Figure S12 in Supporting Information S1 similarly compares NOEM and MSIS 2.1 as a function of latitude and daily  $Kp$ , for September equinox, solar maximum conditions. The patterns are quite similar, with two exceptions. First, as discussed above, the NOEM densities have auroral peaks that are not present in MSIS 2.1. Second, whereas the MSIS 2.1 response at 100 and 110 km saturates above  $Kp = 3-4$ , the NOEM densities continue to increase up to  $Kp = 7$  and above. As a result, the NOEM values are up to a factor of 2 larger than MSIS under very strong geomagnetic activity conditions. We note that in the NOEM development there were only  $\sim 10$  days for which daily  $Kp > 5$  (Marsh et al., 2004, Figure 4a). For the MSIS 2.1 fit, there were  $\sim 150$  such days (Figure 2c) and the saturation appears to be a robust feature of the data (Figure 12 and Figure S6 in Supporting Information S1).

## 7. Comparison With Rocket Experiments

To provide additional independent validation of the MSIS 2.1 results, we compare against five sounding rocket profiles that have been previously published. These are summarized in Table 2. Taken together, these five profiles provide higher altitude data than do the satellite data assimilated into MSIS 2.1, for moderate to high levels of solar activity. As such they can provide a test of MSIS 2.1 for geophysical conditions outside our fitting domain. The first three profiles in Table 2 were first discussed by Siskind and Rusch (1992) and consist of rocket soundings taken at the peak of Solar Cycle 21. The 1990 and 1992 NRL data, from the MUSTANG rocket experiment (Cleary et al., 1995), were presented by Siskind et al. (2004). To date, the MUSTANG data remain the only NO data to extend above 200 km for conditions other than solar minimum. Table 2 provides general details about the date, location, and techniques used but the reader should consider the cited references for specific details.

Figure 16 shows the rocket data compared with both MSIS 2.1 and also a separate photochemical equilibrium calculation based upon MSIS 2.0 temperatures and molecular oxygen densities (which are unchanged in

**Table 2**  
Summary of Rocket Experiments Shown in Figure 16

	1979 U. Colorado	1981 U. Tokyo	1981 U. Colorado	1990 NRL	1992 NRL
Date	7 November 1979	7 September 1981	9 November 1981	30 March 1990	19 March 1992
Time (UT)	0111	0938	2152	1705	1610
Location	$32^\circ\text{N}$ , $106^\circ\text{W}$	$31^\circ\text{N}$ , $131^\circ\text{E}$	$32^\circ\text{N}$ , $106^\circ\text{W}$	$32^\circ\text{N}$ , $106^\circ\text{W}$	$32^\circ\text{N}$ , $106^\circ\text{W}$
Local time	1807	1822	1448	1001	0906
$F_{10.7}$ (sfu)	278	259	239	185	160
$\overline{F}_{10.7}$ (sfu)	225	221	220	185	182
$A_p$	12	5	5	69	4
UV band	$\delta, \gamma$	$\gamma(1,0)$	$\gamma(1,0)$	$\gamma(0,1)$	$\gamma(0,1)$
References	McCoy (1983)	Ogawa et al. (1984)	Siskind et al. (1990)	Cleary et al. (1995) and Siskind et al. (2004)	Cleary et al. (1995) and Siskind et al. (2004)

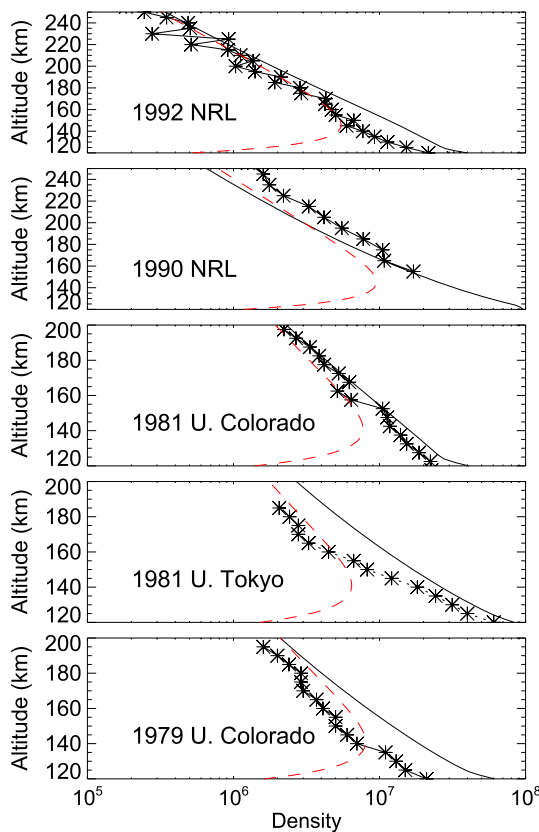


**Figure 16.** (Asterisks) Altitude profiles of nitric oxide (NO) density ( $\text{cm}^{-3}$ ) measured by sounding rockets. The times, locations, and geophysical conditions of each experiment are given in Table 2. (Solid black line) Corresponding MSIS 2.1 NO density profile. (Red dashed line) NO density derived from an NO and  $\text{O}_2$  photochemical equilibrium calculation; see text for details.

MSIS 2.1). As discussed by Siskind et al. (2004), for temperatures above 400–500 K, the temperature-sensitive NO production reaction of  $\text{N}(^4\text{S}) + \text{O}_2$  begins to dominate over the  $\text{N}(^2\text{D}) + \text{O}_2$  channel, which dominates in the colder lower thermosphere. Since NO loss is mainly from recombination with  $\text{N}(^4\text{S})$ , at higher temperatures the NO density can be simply approximated by the following:

$$\text{NO} = \frac{k_1(T)}{k_2} \text{O}_2 \quad (5)$$

where  $k_1$  and  $k_2$  represent the respective (temperature-dependent) production and destruction of NO by  $\text{N}(^4\text{S})$ . By comparing Equation 5 against the NO from MSIS 2.1, we get another independent validation of the MSIS 2.1 results, namely the consistency between the NO and  $\text{O}_2$  fields. Overall, Figure 16 shows good agreement between MSIS 2.1 NO and the data and also good agreement between MSIS 2.1 NO and Equation 5. Note that the model is not constrained to follow Equation 5 but the fact that the model NO and  $\text{O}_2$  densities are both coupled to temperature (in approximately the same way) results in similar vertical gradients and therefore contributes to the model's consistency with Equation 5.

## 8. Summary

NRLMSIS 2.1 incorporates an empirical representation of NO number density in the upper atmosphere, covering altitudes from  $\sim 73$  km to the exobase. The vertical dependence of NO is represented by cubic B-splines up to 122.5 km geopotential height and a modified Bates density profile at higher altitudes, including height-dependent effective mass and a Chapman-like chemical loss term. The model NO density is coupled to the model temperature above 107.5 km. The vertical NO profile parameters are selectively expanded as a function of geographic latitude, day of year, solar activity (via the  $F_{10.7}$  index), geomagnetic activity (via the  $ap$  index), and SZA.

We assimilated six NO data sets (SNOE, MIPAS, ACE, SOFIE, HALOE, and SMR) to tune the model parameters and a seventh (SCIAMACHY) for

independent comparison. The assimilated data collectively include  $\sim 10,000$  unique days of measurement and cover altitudes from 70 to 200 km and years 1991–2020. These data sets provide good coverage of all relevant geophysical conditions (e.g., latitude, season, and solar and geomagnetic activity) with the notable exception of local time. This exception is because all the data sets are either from sun-synchronous satellites or are solar occultation measurements near the terminator, which makes it difficult to resolve local time effects from mutual data biases. The fitting process consisted of sequential least squares estimation on 15 random ensembles of the data; another 15 ensembles were withheld for independent validation. Fortran 90 software to run the model is available in Supporting Information S2 or S3 and in the repository listed in the data availability statement.

Overall, MSIS 2.1 accurately represents most of the climatological variations that consistently occur in the analyzed NO data sets. The results are also consistent with, but greatly extend and broaden, previous analyses of NO density data. The major climatological features of MSIS 2.1 NO include the following:

- A peak density in altitude that occurs between 90 and 110 km
- An overall peak at winter solstice high latitudes, with model densities as high as  $2.5 \times 10^8 \text{ cm}^{-3}$
- As a function of the day of year, the model density maximizes in winter below  $\sim 110$  km and in summer above  $\sim 130$  km.
- Nonlinear increase in log density with  $F_{10.7}$ , concentrated at low latitudes and saturating above  $F_{10.7} \sim 120$  sfu.
- Nonlinear increase in log density with geomagnetic activity, concentrated at high latitudes and saturating above  $Kp = 3$ –4.



The mean deviation between the model and the individual data sets is typically less than 22%. These offsets are height dependent and are larger when specific geophysical conditions are considered. Using the model as a reference for comparing the data sets, we find that the mutual biases among the data sets are typically less than a factor of 2.

We identified the following consistent discrepancies between the NO data and MSIS 2.1; further analysis and model development is needed to resolve these issues:

- The truncated spectral representation of the latitude dependence in the model does not fully represent the behavior of the data during the solstices at 80 km; the data exhibit more of a piecewise linear pattern.
- Below 100 km, the data suggest a small semiannual component in the intra-annual variation, whereas the model is truncated at annual harmonic terms.
- At 80 km, the model does not capture NO density enhancements during strong geomagnetic storms (daily  $K_p > 5$ ) suggested by HALOE and ACE data.
- The data and NOEM suggest a stronger geomagnetic activity response in the Northern Hemisphere than in the Southern Hemisphere; in MSIS 2.1, the response is hemispherically symmetric.
- Siskind et al. (2019) identified a dawn-noon difference in NO density driven by tides. This local time feature is not captured by MSIS 2.1, in part due to the limited local time coverage of the data.

MSIS 2.1 NO density agrees generally well with NOEM under solar moderate and maximum conditions, but at solar minimum, NOEM densities are 2–7 time larger than MSIS 2.1, likely as a result of the more limited amount of solar minimum data used in NOEM. MSIS 2.1 also shows good agreement with independent historical rocket measurements of NO density, and the MSIS 2.1 NO and O<sub>2</sub> densities are consistent with expected chemical balance in the upper thermosphere between the two species.

## List of Acronyms

ACE	Atmospheric Chemistry Experiment
AIM	Aeronomy of Ice in the Mesosphere (satellite mission)
Envisat	Environmental Satellite
FTS	Fourier Transform Spectrometer
HALOE	Halogen Occultation Experiment
MIPAS	Michelson Interferometer for Passive Atmospheric Sounding
MLT	Mesosphere and lower thermosphere
MSIS®	Mass Spectrometer Incoherent Scatter radar
MUSTANG	Middle Ultraviolet Spectral Analysis of Nitrogen Gases
NCAR	National Center for Atmospheric Research
NOEM	Nitric Oxide Empirical Model
NRL	Naval Research Laboratory
ODRPack	Orthogonal Distance Regression Package
SANOMA	SMR Acquired Nitric Oxide Model Atmosphere
SCIAMACHY	SCanning Imaging Absorption SpectroMeter for Atmospheric CHartographY
SMR	Sub-Millimeter Radiometer
SNOE	Student Nitric Oxide Explorer
SOFIE	Solar Occultation For Ice Experiment
SZA	Solar zenith angle
TIME-GCM	Thermosphere-Ionosphere-Mesosphere-Electrodynamics General Circulation Model
UARS	Upper Atmosphere Research Satellite
VMR	Volume mixing ratio

## Data Availability Statement

NRLMSIS 2.1 code and all data samples used in this work are available at <https://map.nrl.navy.mil/map/pub/nrl/NRLMSIS/NRLMSIS2.1/>. The full data sets from which the samples were drawn are available at the following archives: MIPAS (<https://www.imk-asf.kit.edu/english/308.php>), ACE (<http://www.ace.uwaterloo.ca/data.php>),

SOFIE ([http://data.gats-inc.com/sofie/v1.3/mission\\_files/](http://data.gats-inc.com/sofie/v1.3/mission_files/)), SNOE (<https://map.nrl.navy.mil/map/pub/nrl/NRLM-SIS/NRLMSIS2.1/data/>), SMR (<https://odin.rss.chalmers.se/dataaccess>), HALOE (<http://haloe.gats-inc.com/download/index.php>), and SCIAMACHY (<https://zenodo.org/record/581253>).

## Acknowledgments

Work at NRL was supported by the Office of Naval Research (including via the Marine Meteorology and Space Weather Program). S. Bender acknowledges support from the Birkeland Centre for Space Science (BCSS), supported by the Research Council of Norway under the Grant No. 223252/F50. The SCIAMACHY project was a national contribution to the ESA Envisat, funded by the German Aerospace (DLR), the Dutch Space Agency, SNO, and the Belgium Ministry. The ACE mission is supported by the Canadian Space Agency. The IAA team acknowledges financial support from the Spanish Agencia Estatal de Investigación de the Ministerio de Ciencia, Innovación y Universidades through the project PID2019-110689RB-I00 as well as the Centre of Excellence “Severo Ochoa” award to the Instituto de Astrofísica de Andalucía (SEV-2017-0709). Odin is a Swedish-led satellite mission supported by the Swedish National Space Agency (Dnr 20/178 and Dnr 20/88). It is also supported by the European Space Agency as part of the third-party mission program.

## References

- Bailey, S. M., Merkel, A. W., Thomas, G. E., & Rusch, D. W. (2007). Hemispheric differences in polar mesospheric cloud morphology observed by the student nitric oxide explorer. *Journal of Atmospheric and Solar-Terrestrial Physics*, 69(12), 1407–1418. <https://doi.org/10.1016/j.jastp.2007.02.008>
- Barth, C. A., & Bailey, S. M. (2004). Comparison of a thermospheric photochemical model with Student Nitric Oxide Explorer (SNOE) observations of nitric oxide. *Journal of Geophysical Research*, 109(A3), A03304. <https://doi.org/10.1029/2003JA010227>
- Barth, C. A., Mankoff, K. D., Bailey, S. M., & Solomon, S. C. (2003). Global observations of nitric oxide in the thermosphere. *Journal of Geophysical Research*, 108, 1027. <https://doi.org/10.1029/2002JA009458>
- Barth, C. A., Tobiska, W. K., Siskind, D. E., & Cleary, D. D. (1988). Solar-terrestrial coupling: Low-latitude thermospheric nitric oxide. *Geophysical Research Letters*, 15(1), 92–94. <https://doi.org/10.1029/gl015i001p00092>
- Bender, S., Sinnhuber, M., Burrows, J. P., Langowski, M., Funke, B., & López-Puertas, M. (2013). Retrieval of nitric oxide in the mesosphere and lower thermosphere from SCIAMACHY limb spectra. *Atmospheric Measurement Techniques*, 6(9), 2521–2531. <https://doi.org/10.5194/amt-6-2521-2013>
- Bender, S., Sinnhuber, M., Espy, P., & Burrows, J. (2019). Mesospheric nitric oxide model from SCIAMACHY data. *Atmospheric Chemistry and Physics*, 19(4), 2135–2147. <https://doi.org/10.5194/acp-19-2135-2019>
- Bender, S., Sinnhuber, M., von Clarmann, T., Stiller, G., Funke, B., López-Puertas, M., et al. (2015). Comparison of nitric oxide measurements in the mesosphere and lower thermosphere from ACE-FTS, MIPAS, SCIAMACHY, and SMR. *Atmospheric Measurement Techniques*, 8(10), 4171–4195. <https://doi.org/10.5194/amt-8-4171-2015>
- Bernath, P. F. (2017). The atmospheric chemistry experiment (ACE). *Journal of Quantitative Spectroscopy & Radiative Transfer*, 186, 3–16. <https://doi.org/10.1016/j.jqsrt.2016.04.006>
- Boone, C. D., Bernath, P. F., Cok, D., Steffen, J., & Jones, S. C. (2020). Version 4 retrievals for the atmospheric chemistry experiment Fourier transform spectrometer (ACE-FTS) and imagers. *Journal of Quantitative Spectroscopy & Radiative Transfer*, 247, 106939. <https://doi.org/10.1016/j.jqsrt.2020.106939>
- Brasseur, G. P., & Solomon, S. (2005). *Aeronomy of the middle atmosphere* (3rd ed.). Springer. <https://doi.org/10.1007/1-4020-3824-0>
- Chatterjee, S., & Hadi, A. S. (2009). *Sensitivity analysis in linear regression*. Wiley.
- Cleary, D. D., Gnanalingam, S., McCoy, R. P., Dymond, K. F., & Eparvier, F. G. (1995). The middle ultraviolet dayglow spectrum. *Journal of Geophysical Research*, 100(A6), 9729–9739. <https://doi.org/10.1029/94JA03145>
- Emmert, J. T., Drob, D. P., Picone, J. M., Siskind, D. E., Jones, M., Mlynarczyk, M. G., et al. (2020). NRLMSIS 2.0: A whole-atmosphere empirical model of temperature and neutral species densities. *Earth and Space Science*, 8(3), e2020EA001321. <https://doi.org/10.1029/2020EA001321>
- Emmert, J. T., & Picone, J. M. (2010). Climatology of globally averaged thermospheric mass density. *Journal of Geophysical Research*, 115(A9), A09326. <https://doi.org/10.1029/2010JA015298>
- Fischer, H., Birk, M., Blom, C., Carli, B., Carlotti, M., von Clarmann, T., et al. (2008). MIPAS: An instrument for atmospheric and climate research. *Atmospheric Chemistry and Physics*, 8, 2151–2188. <https://doi.org/10.5194/acp-8-2151-2008>
- Fuller-Rowell, T. J. (1993). Modeling the solar cycle change in nitric oxide in the thermosphere and upper mesosphere. *Journal of Geophysical Research*, 98(A2), 1559–1570. <https://doi.org/10.1029/92JA02201>
- Funke, B., García-Comas, M., Glatthor, N., Grabowski, U., Kellmann, S., Kiefer, M., et al. (2022). MIPAS IMK/IAA version 8 retrieval of nitric oxide and lower thermospheric temperature. *Atmospheric Measurement Techniques*, Under Review.
- Gérard, J.-C., & Barth, C. A. (1977). High-latitude nitric oxide in the lower thermosphere. *Journal of Geophysical Research*, 82(4), 674–680. <https://doi.org/10.1029/JA082i004p00674>
- Gómez-Ramírez, D., McNabb, J. W. C., Russell, J. M., III, Hervig, M. E., Deaver, L. E., Paxton, G., & Bernath, P. F. (2013). Empirical correction of thermal responses in the Solar Occultation for Ice Experiment nitric oxide measurements and initial data validation results. *Applied Optics*, 52(13), 2950–2959. <https://doi.org/10.1364/ao.52.002950>
- Gordley, L. L., Russell, J. M., Mickley, L. J., Frederick, J. E., Park, J. H., Stone, K. A., et al. (1996). Validation of nitric oxide and nitrogen dioxide measurements made by the Halogen Occultation Experiment for UARS platform. *Journal of Geophysical Research*, 101(D6), 10241–10266. <https://doi.org/10.1029/95JD02143>
- Harvey, V. L., Datta-Barua, S., Pedatella, N. M., Wang, N., Randall, C. E., Siskind, D. E., & van Cappel, W. E. (2021). Transport of nitric oxide via Lagrangian coherent structures into the top of the polar vortex. *Journal of Geophysical Research: Atmospheres*, 126(11), e2020JD034523. <https://doi.org/10.1029/2020JD034523>
- Hedin, A. E. (1987). MSIS-86 thermospheric model. *Journal of Geophysical Research*, 92(A5), 4649–4662. <https://doi.org/10.1029/JA092iA05p04649>
- Hendrickx, K., Megner, L., Gumbel, J., Siskind, D. E., Orsolini, Y. J., Tyssøy, H. N., & Hervig, M. (2015). Observation of 27 day solar cycles in the production and mesospheric descent of EPP-produced NO. *Journal of Geophysical Research: Space Physics*, 120(10), 8978–8988. <https://doi.org/10.1002/2015JA021441>
- Hendrickx, K., Megner, L., Marsh, D. R., Gumbel, J., Strandberg, R., & Martinsson, F. (2017). Relative importance of nitric oxide physical drivers in the lower thermosphere. *Geophysical Research Letters*, 44(19), 10081–10087. <https://doi.org/10.1002/2017GL074786>
- Hendrickx, K., Megner, L., Marsh, D. R., & Smith-Johnsen, C. (2018). Production and transport mechanisms of no in the polar upper mesosphere and lower thermosphere in observations and models. *Atmospheric Chemistry and Physics*, 18(12), 9075–9089. <https://doi.org/10.5194/acp-18-9075-2018>
- Hervig, M. E., Marshall, B. T., Bailey, S. M., Siskind, D. E., Russell, J. M., III, Bardeen, C. G., et al. (2019). Validation of Solar Occultation for Ice Experiment (SOFIE) nitric oxide measurements. *Atmospheric Measurement Techniques*, 12(6), 3111–3121. <https://doi.org/10.5194/amt-12-3111-2019>
- Houghton, J. T. (1986). *The physics of atmospheres*. Cambridge University Press.
- Jones, M., Forbes, J. M., Hagan, M. E., & Maute, A. (2014). Impacts of vertically propagating tides on the mean state of the ionosphere-thermosphere system. *Journal of Geophysical Research: Space Physics*, 119(3), 2197–2213. <https://doi.org/10.1002/2013JA019744>



- Killeen, T. L., & Roble, R. G. (1986). An analysis of the high-latitude thermospheric wind pattern calculated by a thermospheric general circulation model: 2. Neutral parcel transport. *Journal of Geophysical Research*, 91(A10), 11291–11307. <https://doi.org/10.1029/JA091iA10p11291>
- Kiviranta, J., Pérot, K., Eriksson, P., & Murtagh, D. (2018). An empirical model of nitric oxide in the upper mesosphere and lower thermosphere based on 12 years of Odin SMR measurements. *Atmospheric Chemistry and Physics*, 18(18), 13393–13410. <https://doi.org/10.5194/acp-18-13393-2018>
- Kockarts, G. (1980). Nitric oxide cooling in the terrestrial thermosphere. *Geophysical Research Letters*, 7(2), 137–140. <https://doi.org/10.1029/GL007i002p00137>
- Maeda, S., Fuller-Rowell, T. J., & Evans, D. S. (1989). Zonally averaged dynamical and compositional response of the thermosphere to auroral activity during September 18–24, 1984. *Journal of Geophysical Research*, 94(A12), 16869–16883. <https://doi.org/10.1029/JA094iA12p16869>
- Marsh, D. R., Solomon, S. C., & Reynolds, A. E. (2004). Empirical model of nitric oxide in the lower thermosphere. *Journal of Geophysical Research*, 109(A7), A07301. <https://doi.org/10.1029/2003JA010199>
- McCoy, R. P. (1983). Thermospheric odd nitrogen: 1. NO, N(<sup>4</sup>S), and O(<sup>3</sup>P) densities from rocket measurements of the NO  $\delta$  and  $\gamma$  bands and the O<sub>2</sub> Herzberg I bands. *Journal of Geophysical Research*, 88(A4), 3197–3205. <https://doi.org/10.1029/JA088iA04p03197>
- McHugh, M., Magill, B., Walker, K. A., Boone, C. D., Bernath, P. F., & Russell, J. M., III (2005). Comparison of atmospheric retrievals from ACE and HALOE. *Geophysical Research Letters*, 32(15), L15S10. <https://doi.org/10.1029/2005GL022403>
- Mlynczak, M., Martin-Torres, F. J., Russell, J., Beaumont, K., Jacobson, S., Kozyra, J., et al. (2003). The natural thermostat of nitric oxide emission at 5.3  $\mu$ m in the thermosphere observed during the solar storms of April 2002. *Geophysical Research Letters*, 30(21), 2100. <https://doi.org/10.1029/2003GL017693>
- Mlynczak, M. G., Hunt, L. A., Lopez-Puertas, M., Funke, B., Emmert, J., Solomon, S., et al. (2021). Spectroscopy, gas kinetics and opacity of thermospheric nitric oxide and implications for analysis of SABER infrared emission measurements at 5.3  $\mu$ m. *Journal of Quantitative Spectroscopy and Radiative Transfer*, 268, 107609. <https://doi.org/10.1016/j.jqsrt.2021.107609>
- Natarajan, M., Remsberg, E. E., Deaver, L. E., & Russell, J. M. (2004). Anomalous high levels of NO<sub>x</sub> in the polar upper stratosphere during April, 2004: Photochemical consistency of HALOE observations. *Geophysical Research Letters*, 31(15), L15113. <https://doi.org/10.1029/2004GL020566>
- Nicolet, M., & Aikin, A. C. (1960). The formation of the D region of the ionosphere. *Journal of Geophysical Research*, 65(5), 1469–1483. <https://doi.org/10.1029/JZ065i005p01469>
- Oberheide, J., & Forbes, J. M. (2008). Thermospheric nitric oxide variability induced by nonmigrating tides. *Geophysical Research Letters*, 35(16), L16814. <https://doi.org/10.1029/2008GL034825>
- Ogawa, T., Iwagami, N., & Kondo, Y. (1984). Solar cycle variation of thermospheric nitric oxide. *Journal of Geomagnetism and Geoelectricity*, 36(8), 317–340. <https://doi.org/10.5636/jgg.36.317>
- Pérot, K., & Orsolini, Y. J. (2021). Impact of the major SSWs of February 2018 and January 2019 on the middle atmospheric nitric oxide abundance. *Journal of Atmospheric and Solar-Terrestrial Physics*, 218, 105586. <https://doi.org/10.1016/j.jastp.2021.105586>
- Picone, J. M. (2008). Influence of systematic error on least squares retrieval of upper atmospheric parameters from the ultraviolet airglow. *Journal of Geophysical Research*, 113(A9), A09306. <https://doi.org/10.1029/2007JA012831>
- Picone, J. M., Hedin, A. E., Drob, D. P., & Aikin, A. C. (2002). NRLMSISE-00 empirical model of the atmosphere: Statistical comparisons and scientific issues. *Journal of Geophysical Research*, 107(A12), 1468. <https://doi.org/10.1029/2002JA009430>
- Randall, C. E., Harvey, V. L., Holt, L. A., Marsh, D. R., Kinnison, D., Funke, B., & Bernath, P. F. (2015). Simulation of energetic particle precipitation effects during the 2003–2004 Arctic winter. *Journal of Geophysical Research: Space Physics*, 120(6), 5035–5048. <https://doi.org/10.1002/2015JA021196>
- Randall, C. E., Harvey, V. L., Singleton, C. S., Bailey, S. M., Bernath, P. F., Codrescu, M., et al. (2007). Energetic particle precipitation effects on the Southern Hemisphere stratosphere in 1992–2005. *Journal of Geophysical Research*, 112(D8), D08308. <https://doi.org/10.1029/2006JD007696>
- Roble, R. G. (1996). The NCAR thermosphere-ionosphere-mesosphere-electrodynamics general circulation model (TIME-GCM). In *Step handbook on ionospheric models* (pp. 281–288). Utah State University.
- Roble, R. G., & Ridley, E. C. (1994). A thermosphere-ionosphere-mesosphere-electrodynamics general circulation model (TIME-GCM): Equinox solar cycle minimum simulations (30–500 km). *Geophysical Research Letters*, 21(6), 417–420. <https://doi.org/10.1029/93GL03391>
- Sinnhuber, M., Friederich, F., Bender, S., & Burrows, J. P. (2016). The response of mesospheric NO to geomagnetic forcing in 2002–2012 as seen by SCIAMACHY. *Journal of Geophysical Research: Space Physics*, 121(4), 3603–3620. <https://doi.org/10.1002/2015JA022284>
- Siskind, D. E., Barth, C. A., & Cleary, D. D. (1990). The possible effect of solar soft X-rays on thermospheric nitric oxide. *Journal of Geophysical Research*, 95(A4), 4311–4317. <https://doi.org/10.1029/JA095iA04p04311>
- Siskind, D. E., Barth, C. A., Evans, D. S., & Roble, R. G. (1989). The response of thermospheric nitric oxide to an auroral storm: 2. Auroral latitudes. *Journal of Geophysical Research*, 94(A12), 16899–16911. <https://doi.org/10.1029/JA094iA12p16899>
- Siskind, D. E., Barth, C. A., & Russell, J. M., III (1998). A climatology of nitric oxide in the mesosphere and thermosphere. *Advances in Space Research*, 21(10), 1353–1362. [https://doi.org/10.1016/s0273-1177\(97\)00743-6](https://doi.org/10.1016/s0273-1177(97)00743-6)
- Siskind, D. E., McArthur, J. J., Drob, D. P., McCormack, J. P., Hervig, M. E., Marsh, D. R., et al. (2019). On the relative roles of dynamics and chemistry governing the abundance and diurnal variation of low-latitude thermospheric nitric oxide. *Annals of Geophysics*, 37(1), 37–48. <https://doi.org/10.5194/angeo-37-37-2019>
- Siskind, D. E., Nedoluha, G. E., Randall, C. E., Fromm, M., & Russell, J. M., III (2000). An assessment of southern hemisphere stratospheric NO<sub>x</sub> enhancements due to transport from the upper atmosphere. *Geophysical Research Letters*, 27(3), 329–332. <https://doi.org/10.1029/1999GL010940>
- Siskind, D. E., Picone, J. M., Stevens, M. H., & Minschwaner, K. (2004). Middle and upper thermospheric odd nitrogen: 1. A new analysis of rocket data. *Journal of Geophysical Research*, 109(A1), A01303. <https://doi.org/10.1029/2003JA009943>
- Siskind, D. E., & Rusch, D. W. (1992). Nitric oxide in the middle to upper thermosphere. *Journal of Geophysical Research*, 97(A3), 3209–3217. <https://doi.org/10.1029/91JA02657>
- Siskind, D. E., Strickland, D. J., Meier, R. R., Majeed, T., & Eparvier, F. G. (1995). On the relationship between the solar soft X-ray flux and thermospheric nitric oxide: An update with an improved photoelectron model. *Journal of Geophysical Research*, 100(A10), 19687–19694. <https://doi.org/10.1029/95JA01609>
- Smith, A. K., Garcia, R. R., Marsh, D. R., & Richter, J. H. (2011). WACCM simulations of the mean circulation and trace species transport in the winter mesosphere. *Journal of Geophysical Research*, 116(D20), D20115. <https://doi.org/10.1029/2011JD016083>
- Solomon, S., Crutzen, P. J., & Roble, R. G. (1982). Photochemical coupling between the thermosphere and the lower atmosphere: 1. Odd nitrogen from 50 to 120 km. *Journal of Geophysical Research*, 87(C9), 7206–7220. <https://doi.org/10.1029/JC087iC09p07206>
- Stevens, M. H. (1995). Nitric oxide  $\gamma$  band fluorescent scattering and self-absorption in the mesosphere and lower thermosphere. *Journal of Geophysical Research*, 100(A8), 14735–14742. <https://doi.org/10.1029/95JA01616>

- Tapping, K. F. (2013). The 10.7 cm solar radio flux (F10.7). *Space Weather*, 11(7), 394–406. <https://doi.org/10.1002/swe.20064>
- Zhang, Y., & Paxton, L. J. (2021). Storm-time neutral composition changes in the upper atmosphere. In W. Wang, Y. Zhang, & L. J. Paxton (Eds.), *Upper atmosphere dynamics and energetics*. <https://doi.org/10.1002/9781119815631.ch7>
- Zwolak, J. W., Boggs, P. T., & Watson, L. T. (2007). Algorithm 869: ODRPACK95, 2007: A weighted orthogonal distance regression code with bound constraints. *Association for Computing Machinery*, 33(4), 27. <https://doi.org/10.1145/1268776.1268782>

## References From the Supporting Information

- Emmert, J. T., Richmond, A. D., & Drob, D. P. (2010). A computationally compact representation of Magnetic-Apex and Quasi-Dipole coordinates with smooth base vectors. *Journal of Geophysical Research*, 115(A8), A08322. <https://doi.org/10.1029/2010JA015326>
- Richmond, A. D. (1995). Ionospheric electrodynamics using magnetic apex coordinates. *Journal of Geomagnetism and Geoelectricity*, 47(2), 191–212. <https://doi.org/10.5636/jgg.47.191>